Surface Energy Budget, Albedo and Thermal Inertia at Jezero Crater, Mars, as Observed from the Mars 2020 MEDA Instrument

G. M. Martínez[1,2], E. Sebastián[3], A. Vicente-Retortillo[3,2], M. D. Smith[4], J. R. Johnson[5], E. Fischer[2], H. Savijärvi[6], D. Toledo[7], R. Hueso[8], L. Mora-Sotomayor[3], H. Gillespie[1], A. Munguira[8], A. Sánchez-Lavega[8], M. T. Lemmon[9], F. Gómez[3], J. Polkko[10], L. Mandon[11], V. Apéstigue[6], I. Arruego[6], M. Ramos[12], P. Conrad[13], C. E. Newman[14], M. de la Torre-Juarez[15], F. Jordan[3], L. K. Tamppari[15], T. H. McConnochie[9], A.-M. Harri[10], M. Genzer[10], M. Hieta[10], M.-P. Zorzano[3], M. Siegler[16], O. Prieto[3], A. Molina[3], and J. A. Rodríguez-Manfredi[3]

[1]Lunar and Planetary Institute, Universities Space Research Association, Houston, TX, USA
[2]University of Michigan, USA
[3]Centro de Astrobiología (INTA-CSIC), Spain
[4]NASA Goddard Space Flight Center, USA
[5]John Hopkins University/APL, USA
[6]University of Helsinki, Finland
[7]Instituto Nacional de Técnica Aeroespacial, Spain
[8] Universidad del País Vasco/Euskal Herriko Unibertsitatea, Spain
[9]Space Science Institute, USA
[10]Finnish Meteorological Institute, Finland
[11]Laboratoire d'Etudes Spatiales et d'Instrumentation en Astrophysique, Observatoire de Paris-PSL, France
[12]Universidad de Alcalá de Henares, Spain
[13]Carnegie Institution for Science, USA
[14]Aeolis Research, USA
[15]Jet Propulsion Laboratory, California Institute of Technology, USA
[16]Planetary Science Institute, USA.

Key Points:

- MEDA allows the first *in-situ* determination of the surface radiative budget on Mars, providing key constraints on numerical models.
- MEDA allows the direct determination of thermal inertia and albedo, providing ground-truth to satellite retrievals.
- Albedo shows a strong non-Lambertian behavior, with minimum values at noon and higher values towards sunrise and sunset.

Abstract

The Mars Environmental Dynamics Analyzer (MEDA) on board Perseverance includes first-of-their-kind sensors measuring the incident and reflected solar flux, the downwelling atmospheric IR flux, and the upwelling IR flux emitted by the surface. We use these measurements for the first 350 sols of the Mars 2020 mission (L_s ~ 6°–174° in Martian Year 36) to determine the surface radiative budget on Mars, and to calculate the broadband albedo (0.3–3 μm) as a function of the illumination and viewing geometry. Together with MEDA measurements of ground temperature, we calculate the thermal inertia for homogeneous terrains without the need for numerical models. We found that: (1) the observed downwelling atmospheric IR flux is significantly lower than model predictions. This is likely caused by the strong diurnal variation in aerosol opacity measured by MEDA, which is not accounted for by numerical models. (2) The albedo presents a marked non-Lambertian behavior, with lowest values near noon and highest values corresponding to low phase angles (i.e., Sun behind the observer). (3) Thermal inertia values ranged between 180 (sand dune) and 605 (bedrock-dominated material) SI units. (4) Averages across Perseverance' traverse of albedo and thermal inertia (spatial resolution of ~3–4 m^2) are in very good agreement with collocated retrievals of thermal inertia from THEMIS (spatial resolution of 100 m per pixel) and of bolometric albedo in the 0.25–2.9 μm range from (spatial resolution of ~300 km^2). The results presented here are important to validate model predictions and provide ground-truth to orbital measurements.

Plain Language Summary

We analyzed first-of-their-kind measurements from the weather station on board NASA's Perseverance rover. These include the incident solar radiation and the amount of it that is reflected by the surface, as well as the thermal atmospheric forcing (greenhouse effect) and the thermal heat released by the surface. These measurements comprise the radiant energy budget, which is fundamental to understanding Mars' weather through its impact on temperatures. From the solar measurements, we obtained the surface reflectance for a variety of illuminating and viewing geometries. We found that the thermal atmospheric forcing is weaker than expected from models, likely because of the strong diurnal variation in atmospheric aerosols observed by the rover, which is not accounted for by models. We also found that the surface reflectance is not uniform from all directions, but that it decreases when the Sun is highest in the sky (near noon) and increases when the Sun is directly behind the observer (sunset and sunrise), and thus the shadows cast by their roughness elements (e.g., pores, pits) are minimized. Because models neither consider diurnal variations in atmospheric aerosols nor in the surface reflectance, the results presented here are important to validate model predictions for future human exploration.

Outline (to be removed if manuscript accepted for publication)

1. Introduction

The Mars 2020 Perseverance rover landed at Jezero Crater (77.5945°E, 18.3628°N, -2656 m) on February 18, 2021, corresponding to a solar longitude (L_s) of ~5° in Martian Year (MY) 36. It carries seven science instruments to fulfill four science goals: (1) understand the geology of the landing site, (2) identify ancient habitable environments and look for preserved biosignatures, (3) collect and document samples for future Earth return, and (4) enable future human exploration of Mars (Farley et al., 2021).

Among these instruments, the Mars Environmental Monitoring Station (MEDA) is a meteorological station selected by NASA to help achieve mission science goal 4 (Rodríguez-Manfredi et al., 2021; Newman et al., 2022). In particular, the main programmatic objectives of MEDA are to: (1) validate global atmospheric models by taking surface weather measurements, and (2) characterize dust size and morphology to understand its effects on the operation of surface assets and human health. Additionally, MEDA provides environmental context in support of science goals 1–3 and the flights of Ingenuity, the helicopter included in the mission as a technology demonstrator.

To achieve its objectives, MEDA carries six sensor packages: the Thermal Infrared Sensor (TIRS; Pérez-Izquierdo et al., 2018; Sebastián et al., 2020, 2021), the Radiation and Dust Sensor (RDS; Apéstigue et al., 2022), the Atmospheric Temperature Sensor (ATS), the Pressure Sensor (PS), (5) the Relative Humidity Sensor (HS), and the Wind Sensor (WS). In addition, the RDS incorporates an upward-viewing wide-angle camera to image the sky, informally called SkyCam. Among these, TIRS and RDS are providing first-of-their-kind measurements from the surface of Mars, and are the main the focus of this article.

RDS and TIRS allow the determination of the surface radiative budget on Mars for the first time through measurements of the incident (SW_d; 0.19–1.2 μm) and reflected (SW_u; 0.3–3 μm) solar flux, the downwelling atmospheric IR flux (LW_d; 6.5–30 μm), and the upwelling IR flux emitted by the surface (LW_u; 6.5–30 μm). As required in quantifications of the radiative energy budget, we explain in Section 3 how to extend these measurements to the entire shortwave (0.19–5 μm) and longwave range (5–80 μm). The surface radiative budget of Mars is fundamental to understanding its weather and climate through its impact on the thermal structure and atmospheric circulations (e.g., Creecy et al., 2022). Moreover, RDS and TIRS measurements are critical to validate and improve predictive capabilities of numerical models. Therefore, determination of the surface radiative budget is critical to achieve MEDA's first programmatic objective. Before Perseverance, this budget has been estimated using a combination of *in-situ* measurements and numerical models (Martínez et al., 2021, and references therein). Here, we expand and improve upon previous studies by analyzing *in-situ* measurements of the surface radiative budget around the clock.

Together with the radiative fluxes, the turbulent heat flux (H_0) and the latent heat flux (L_f) make up the surface energy budget (SEB), which can be expressed as $G = SW_d - SW_u + LW_d - LW_u - H_0 - L_f$. Here, G represents the net heat flux into the ground, and $R_n = SW_d - SW_u + LW_d - LW_u$ is the net radiative flux derived from MEDA measurements (sign convention defined in Section 3). Although not measured, H_0 and L_f can be estimated using combined MEDA measurements from TIRS, ATS, WS, PS, and HS using similarity theories (Section 3). These two terms play, at most,

a minor role in the Martian SEB (Sutton et al., 1978; Haberle et al., 1993; Martínez et al., 2014; 2021; Savijärvi et al., 2022, this issue). Therefore, MEDA provides a reasonable approximation to the SEB at Jezero.

Another novel capability of MEDA is the direct determination of the broadband (0.3–3 μm) albedo through measurements of the incident and reflected solar flux (see Section 3.2 for the definition of albedo used in this article). Albedo is a key parameter in the radiative energy budget, thus affecting the local weather and climate (Kahre et al., 2005; Fenton et al., 2007). In previous surface-based missions, the albedo has been calculated either from radiometrically calibrated images taken by panoramic cameras (Rice et al., 2018; Bell et al., 2008), or by using numerical models to best fit observed values of ground temperature (Vasavada et al., 2017; Piqueux et al., 2021). Additionally, telescope and satellite observations have been used to retrieve albedo globally across the planet (e.g., Kieffer et al., 1977; Christensen 1988; Christensen et al., 2001; Vincendon et al., 2015). In either case, the temporal coverage was limited given the nature of the observations, with one image or satellite retrieval per day and location at best. Accordingly, the geometry of incident and reflected solar fluxes was limited, complicating assessments of the Lambertian (isotropically scattering surface) approximation, which has been assumed in these studies.

Here we expand upon previous studies and obtain broadband albedo values for a variety of illumination and viewing geometries, which allows us to study the degree to which the surface materials depart from ideal Lambertian scattering (Section 4). This is important for improving predictive capabilities of mesoscale and global models (Montmessin et al., 2007; Fenton et al., 2007), which typically incorporate albedo variations in subseasonal time scales (Haberle et al., 1993; Kahn et al., 2005; Fenton et al., 2007, Geissler et al., 2016), but not in diurnal timescales arising from non-Lambertian behavior. Similarly, surface-based and satellite retrievals of thermal inertia (Putzig et al., 2005; Fergason et al., 2006; Vasavada et al., 2017; Savijärvi et al., 2020; Piqueux et al., 2021) typically consider a constant value of albedo throughout the day, and thus also may benefit from non-Lambertian considerations.

Furthermore, MEDA measurements allow for the direct estimation of thermal inertia assuming homogeneous terrains within the ground temperature sensor's field of view (Section 3). Thermal inertia is an important geophysical property of the terrain, which modulates the amount of energy flux that is transported into the subsurface, and thus determines surface and shallow subsurface temperatures. In previous studies, thermal inertia has been obtained by fitting thermal models to measurements of ground temperature retrieved from satellite observations (e.g., Kieffer et al., 1977; Mellon et al., 2000; Fergason et al., 2006a; Fergason et al., 2012; Gondet et al., 2013), measured by surface-based missions (e.g., Fergason et al., 2006b; Hamilton et al., 2014; Martínez et al., 2014; Vasavada et al., 2019; Piqueux et al., 2021), or using both datasets coincidently (Edwards et al., 2018; Christian et al., 2021). In either case, a thermal model is fed with key parameters such as aerosol opacity, pressure, and albedo, among others, to simulate the SEB at the surface. Then, these models solve the heat conduction at the ground for homogeneous or heterogeneous terrains using the simulated SEB as the upper boundary condition, obtaining the thermal inertia by best fitting their outputs to measured values of ground temperature.

Here we obtain thermal inertia directly by using MEDA measurements of ground temperature (T_g), albedo and SEB assuming homogeneous terrains. An in-depth analysis of the differences between thermal inertia values derived assuming heterogeneous versus homogeneous terrains is presented in Savijärvi et al. (2022; this issue).

In this article, we report results of the surface energy budget, broadband albedo, and thermal inertia for the first 350 sols of the M2020 mission, corresponding to L_s 6°–174° in MY 36. The structure of the article is the following. Section 2 describes MEDA observations, with focus on TIRS and RDS. Section 3 explains the methods to calculate each term of the surface energy budget (Section 3.1), albedo (Section 3.2) and thermal inertia (Section 3.3). Section 4 shows the results, and it is also divided into three subsections devoted to the thermal inertia (Section 4.1), surface energy budget (Section 4.2) and albedo (Section 4.3). Section 5 discusses discrepancies between measured and modeled values of the downwelling atmospheric IR flux. Section 6 contains the summary and conclusions.

2. The MEDA Instrument

Here, we explain the measuring strategy of MEDA and describe each of its six sensor packages, with focus on TIRS and RDS.

The nominal measuring strategy of MEDA began on sol 15 (Ls ~ 12°). It consists of 1h-and-5'-long blocks starting at odd Local Mean Solar Times (LMST) hours on odd sols, and on even LMST hours on even sols (Fig. 1). This ensures that the beginning of each hour is covered on every sol, and that each full hour is covered every two sols. Additional or extended blocks are added when mission resources allowed (data volume and power). During nominal or extended blocks, each MEDA sensor is typically measuring at 1 Hz, although a higher frequency of 2 Hz has been used occasionally by a few sensors (e.g., ATS) to better characterize turbulent phenomena (de la Torre-Juarez et al., 2022; this issue). In parallel, a few SkyCam images are taken on each sol (typically between 3 and 4).

TIRS is the first *in-situ* Martian IR radiometer including upward- and downward-looking channels (Pérez-Izquierdo et al., 2018; Sebastián et al., 2020, 2021). TIRS measures the downwelling atmospheric IR flux (IR1), the air temperature from an atmospheric layer with peak emission at 40 m (IR2; Smith et al., 2006), the reflected (upwelling) solar flux (IR3), the upwelling IR flux emitted by the surface (IR4), and the surface brightness temperature (IR5) (Table 1). IR1, IR2, IR3, and IR4 provide novel measurements on Mars, while IR5 complements previous measurements of surface brightness temperatures taken by the Rover Environmental Monitoring Station (REMS) on board the Mars Science Laboratory (MSL) mission (Sebastián et al., 2010), and by the HP^3 instrument on board InSight (Spohn et al., 2018).

TIRS is mounted on the rover sensing mast (RSM) at a height of 1.5 m, and it is located 75° clockwise in the horizontal plane with respect to Z-axis local frame (with +X defined along the forward direction and +Y pointing to the right of the rover). The field of view (FoV) of the downward-looking channels covers an ellipsoid area of 3–4 m^2, whose center is ~3.75 m away from the M2020 Radioisotope Thermoelectric Generator to avoid thermal contamination (Fig. 2). Most of the signal comes from the central part of the ellipsoid, where the detectors have the highest responsivity (Sebastian et al., 2020). Due to the smaller area covered by TIRS as

compared with the MSL/REMS ground temperature sensor (3–4 m^2 versus ~100 m^2), lateral heterogeneities in thermal inertia and albedo are expected to be more prevalent at MSL than at the M2020 landing site.

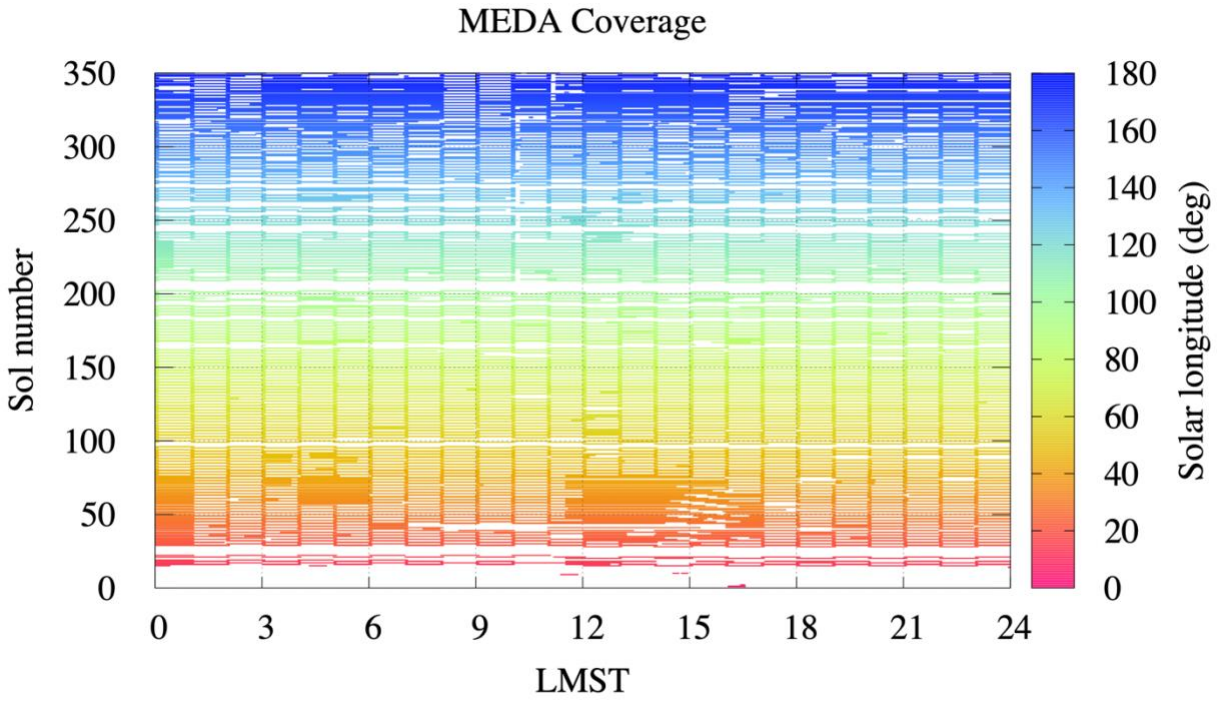

Figure 1. Temporal coverage of MEDA as a function of LMST and sol number, with Ls shown with color code. Sols with no coverage correspond to periods when MEDA was off due to various reasons, while the dense cloud of reddish points between 11:00 and 17:00 LMST in sols 31–77 correspond to extra measurements taken in support of the first Ingenuity flights.

Channel	**IR1**	**IR2**	**IR3**	**IR4**	**IR5**
Measurement	LW_d	T_a	SW_u	LW_u	T_g
Band (µm)	6.5–30	14.5–15.5	0.3–3	6.5–30	8–14
Field of View	±20° H ±10° V	±20° H ±10° V	±20° H ±10° V	±20° H ±10° V	±20° H ±10° V
Pointing Angle	+35°	+35°	-35°	-35°	-35°
Accuracy	< 6.9 W/m^2	±2.83 K	< 9.6 W/m^2	< 3.3 W/m^2	±0.75 K
Resolution	±0.18 W/m^2	±0.45 K	±0.1 W/m^2	±0.13 W/m^2	±0.08 K

Table 1. Specifications and geometrical description of TIRS. LW_d is the downwelling atmospheric IR flux, T_a is the air temperature at about 40 m, SW_u is the solar flux reflected by the surface, LW_u is the upwelling IR flux emitted by the surface, and T_g is the surface brightness temperature. For the accuracy and resolution of IR1 and IR4, a hemispherical field of view and the full IR range was considered in pre-flight calibrations (Sebastián et al., 2020; 2021). For IR3, a hemispherical field of view was also considered based on laboratory and field calibrations (Rodríguez-Manfredi et al., 2021).

The RDS is located on the rover deck (Fig. 2). It includes 16 photodiodes and the SkyCam to take images of the sky in the 0.6-0.8 μm range (Apéstigue et al., 2022). Among the 16 photodetectors, 8 point toward the zenith (TOP) in different spectral bands ranging from the UV to the near IR, while 8 point sideways (LAT) in the 0.75 ± 0.01 μm range, each separated 45° from the next in the horizontal plane to cover 360°. LAT1 sensor is blinded, and it is used to evaluate possible photodetector degradation. RDS TOP photodetectors complement and expand upon previous solar flux measurements taken by the MSL/REMS instrument, which only cover the UV range (Vicente-Retortillo et al., 2020). SkyCam has strong heritage from the hazard cameras (HazCams) used in the MSL and Mars Exploration Rover (MER) missions (Maki et al., 2003, 2012).

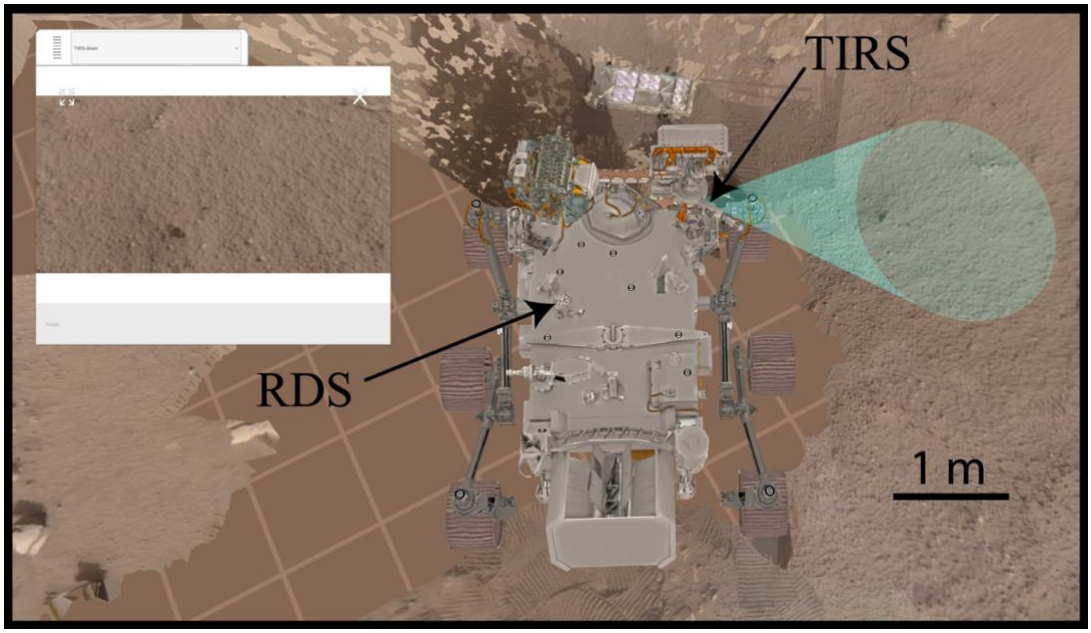

Figure 2. Field of view of the downward-looking TIRS channels IR3, IR4 and IR5 (shaded green area) on sol 30. For terrains with no tilt, it covers an ellipsoidal area of ~3–4 m^2. The arrows point toward the location of TIRS on the remote sensing mast, which is placed 75° clockwise from the rover forward direction, and of the RDS on the rover deck. A zoomed-in view of TIRS' field of view is shown on the top left insert.

In this work, we only use RDS measurements from the panchromatic channel (TOP 7), which measures the downwelling solar flux in the 0.19–1.2 μm range with a hemispherical FoV of ±90°, and with an accuracy and resolution of 5.6% and 0.0221 W m^{-2}, respectively. The reader is referred to Toledo et al. (2022; this issue) for science results of RDS using TOP and LAT channels combined.

Measurements of TIRS/IR1 (LW_d), TIRS/IR3 (SW_u), TIRS/IR4 (LW_u) and RDS/TOP7 (SW_u) allow the determination of the net radiative energy budget, R_n. In addition, we use measurements from other MEDA sensors to provide environmental context and to estimate the turbulent heat flux. We briefly describe each of these sensors below.

The ATS includes five atmospheric sensors based on thermocouples. Three of them (ATS1, ATS2, and ATS3) are located on the RSM at 1.45 m above the ground, separated ~120° from each other in the horizontal plane to ensure that at least one is always upwind from rover thermal interferences. Two other thermocouples (ATS 4 and ATS5) are attached to the sides of the rover at a height of 0.84 m. All thermocouples have an accuracy and resolution better than 1 and 0.01 K, respectively (Rodríguez-Manfredi et al., 2021). Here, we use measurements from ATS1, ATS2 and ATS3, which typically provide similar values and are less affected by the contamination from the rover (Munguira et al., 2022).

The WS consists of two booms located on the RSM at ~1.5 m height, separated ~120° from each other in the horizontal plane to mitigate rover hardware interferences (Rodríguez-Manfredi et al., 2021). Data from both booms are combined to produce horizontal wind speed and direction values of the highest confidence, with accuracies of ±1 m/s and a resolution of 0.5 m/s for wind speeds < 10 m/s, and 10% of the measurement and 0.1 m/s for wind speeds between 10 and 40 m/s. The WS was damaged by a dust devil during the regional dust storm around sols 312–318 (Ls 152°–156°) (Hueso et al., 2022, this issue; Lemmon et al., 2022, this issue; Viúdez-Moreiras et al., 2022a, 2022b, this issue). Thus, WS measurements of the highest confidence are only available for the first 313 sols of the mission (Fig. S1). In addition, the wind sensor had to be turned off during orbital communication passes, which reduces its time coverage compared to other MEDA sensors (Fig. S1).

The PS is located in a temperature-controlled box inside the rover, and it is connected to the atmosphere through a pipe (Sánchez-Lavega et al., 2022, this issue; Rodríguez-Manfredi et al., 2021). It measures the atmospheric pressure with an estimated accuracy ~3.5 Pa and a resolution of 0.13 Pa. In combination with the ATS, these sensors can be used to estimate the atmospheric density, which is an important quantity in support of the Mars Oxygen In-Situ Resource Utilization Experiment (MOXIE) instrument on board M2020, and also to estimate the turbulent heat flux (Section 3).

The HS is located on the RSM at 1.5 m height from the ground (Polkko et al., 2022; this issue), and it was calibrated to provide values of the relative humidity (*RH*) with respect to ice with an uncertainty lower than 4.5% for temperatures above 203 K, and lower than 6% down to 190 K. The precision of the HS is better than 0.02% in *RH*. Due to some inflight maintenance, only HS measurements taken after sol 80 (Ls ~ 43.5°) are suitable for scientific investigations. The HS can also be used to estimate the water vapor pressure at 1.5 m as $e = RH \times e_s(T_b)$, where T_b is the temperature of the HS measured directly from the HUMICAP chip, and e_s is the saturation vapor pressure over ice (Savijärvi et al., 2010). Similarly, the water vapor volume mixing ratio can be estimated as $VMR = e/P = (RH \times e_s(T_b))/P$, where P is the atmospheric pressure provided by the PS. In both cases, e and VMR can be obtained reliably only when $RH > 2$ %, roughly corresponding to LMST between 07:00 and 17:00 (Fig. S2g). The reader is referred to Polkko et al. (2022; this issue) for further details on the science capabilities of the HS.

To provide context for the results shown in Section 4, Fig. 3 shows the subseasonal evolution of the environmental conditions across Perseverance's traverse for the first 350 sols of the M2020 mission. Diurnal variations of the same quantities are shown in Fig. S2.

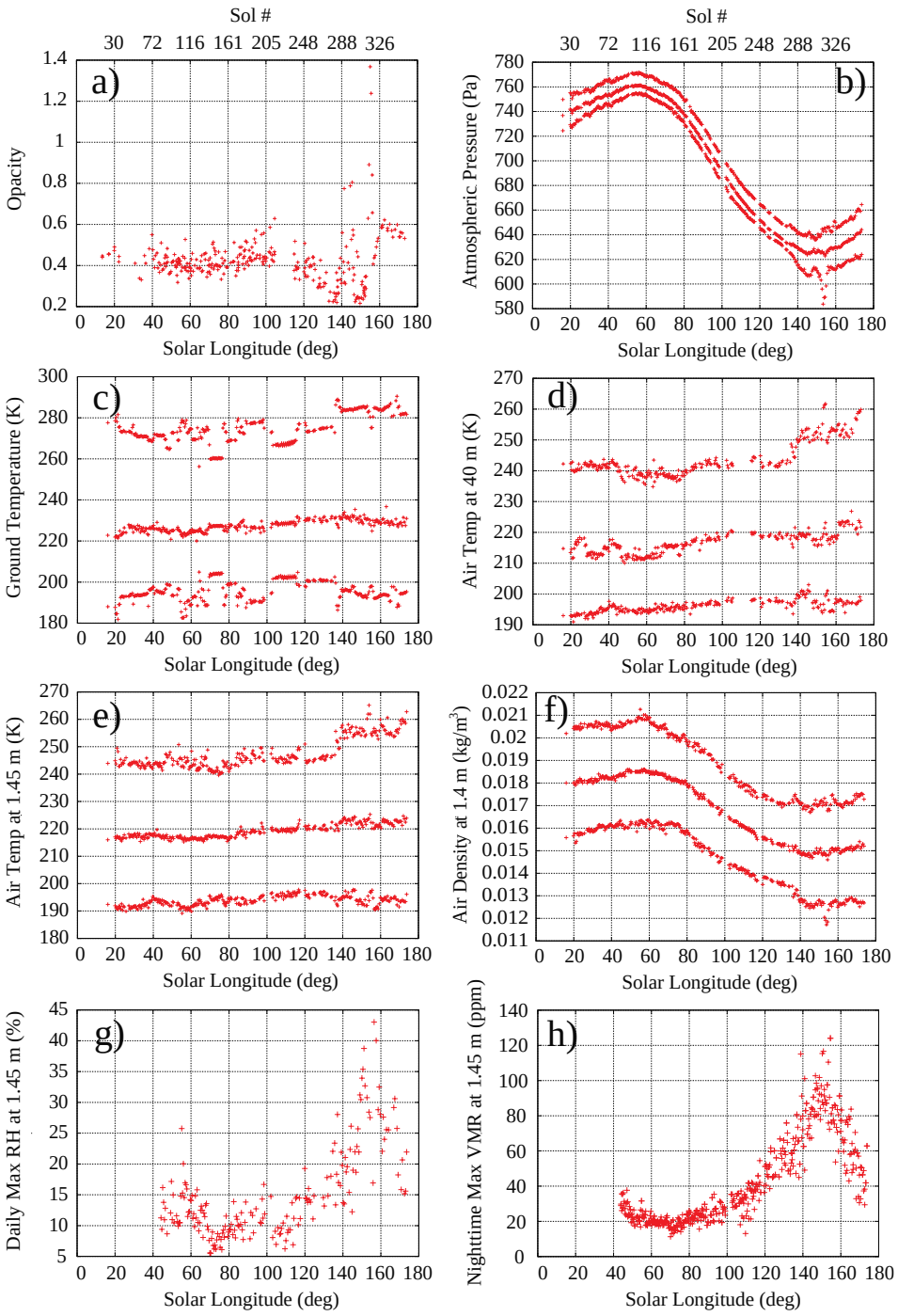

Figure 3. Environmental conditions during the first 350 sols of the M2020 mission, which roughly cover the entire Martian aphelion season. **(a)** Aerosol opacity at 0.88 μm retrieved by the Mastcam-Z instrument. **(b)** Daily maximum, mean, and minimum atmospheric pressure. **(c)** Daily maximum, mean, and minimum ground temperature. **(d)** Daily maximum, mean, and minimum air temperature at about 40 m. **(e)** Daily maximum, mean, and minimum air temperature at 1.45 m, where only ATS1, ATS2, and ATS3 have been considered. **(f)** Daily maximum, mean, and minimum atmospheric density at 1.45 m. **(g)** Daily maximum RH. **(h)** Nighttime maximum water vapor VMR.

3. Methods

In this section we explain the methods to calculate each term of the surface energy budget (Section 3.1), hemispheric albedo (Section 3.2) and thermal inertia (Section 3.3) using MEDA observations.

3.1. Surface Energy Budget

The surface energy budget can be expressed as

$$G = (SW_d - SW_u + LW_d - LW_u) - (H_0 + L_f), \quad (1)$$

where G represents the net heat flux into the ground, $R_n = SW_d - SW_u + LW_d - LW_u$ the net surface radiative flux, and H_0 and L_f the turbulent and latent heat flux. Following the convention in Garrat (1992), radiative fluxes are plugged into this equation as positive values, whereas H_0 and L_f fluxes can be plugged in as positive or negative depending on whether they are directed away (cooling) from or toward (warming) the surface, respectively.

The spectral boundary between solar (SW_d and SW_u) and IR (LW_d and LW_u) fluxes is set at 5 μm (Wolff et al., 2017), which may cause inaccuracies smaller than 0.5% in the individual terms; this effect is in turn partially compensated due to the subtraction of downwelling and upwelling terms.

3.1.1. Shortwave Flux

3.1.1.1. Downwelling Solar Flux: RDS/TOP7

The most processed RDS/TOP7 measurements available in the NASA Planetary Data System (PDS) are 'Calibrated Data' (*CAL_RDS* files). To obtain SW_d from these measurements, we took the following steps: (1) correction for the angular response, (2) extension from 0.19–1.2 μm to 0.19–5 μm (atmospheric CO_2 blocks wavelengths < 0.19 μm; e.g., Vicente-Retortillo et al., 2015), and (3) correction for the amount of dust deposited on the photodiode. Moreover, we discard measurements: (4) affected by shadows cast by the RSM, and (5) taken when the RDS/TOP7 was saturated.

The angular response of the RDS/TOP7 channel is available in the Supporting Information (SI) in the form of a look-up table as a function of the aerosol opacity (τ) and solar zenith angle (*SZA*) stored in ASCII format (supporting dataset, ds01). Aerosol opacity values (Fig. 3a; Fig. S2a) are available in the Data Availability Statement, while *SZA* values are available in the PDS as 'Derived Data' (*DER_ANCILLARY* files). To convert RDS/TOP7 fluxes from 0.19–1.2 μm to 0.19–5 μm, we use a look-up table (available in the SI in ASCII format; ds02, 7th column) generated by our COMIMART radiative model (Vicente-Retortillo et al., 2015), which also depends on the aerosol opacity and, more modestly, on the *SZA*. Finally, we quantify the effect of dust deposited on the RDS/TOP7 through the calculation of a dust correction factor (DCF). This quantity is defined as the fraction of the incoming flux that reaches the photodiode through dust accumulated on the sensor, with respect to the fraction at the beginning of the mission. By using COMIMART, aerosol opacity retrieved from Mastcam-Z, RDS/TOP7 measurements, and the methodology developed in Vicente-Retortillo et al. (2018; 2020), we estimated an averaged DCF of 0.94 over the first 270 sols of the mission (i.e., 94% of the solar flux is transmitted through the dust accumulated on the window of the sensor). Interestingly, the DCF stayed

reasonably constant at 0.94 throughout this period (Ls in 6°–130°), including the first sols of the mission. This suggests that some dust might have deposited on the RDS/TOP7 window during landing. This hypothesis is further supported by an in-flight recalibration of TIRS performed during the first few sols, which resulted in a degradation of ~9% in the signal measured by the upward-looking TIRS channels.

In addition to the corrections explained above, we discard measurements affected by shadows cast by the RSM. At the time of this writing, there are no flags available in the 'CAL_RDS' files indicating whether or not an RDS/TOP7 measurement is affected by such shadows. Thus, we discard these measurements manually from visual inspection. Moreover, we discard measurements when the RDS/TOP7 was saturated, which can occur under two different scenarios: in the vicinity of sunrise when the RDS was operating in high gain mode, and in the vicinity of noon between sols ~270 (Ls ~131°) and 350 (Ls ~174°) when the incident solar flux was higher than the upper bound of the range established in pre-flight calibrations on Earth (Fig. S3). During this period (sols 270–350), we used COMIMART fed with aerosol opacity values from Mastcam-Z to simulate near-noon values of SW_d (more details in Section 3.2). As with the shadows, there are no flags associated to saturated measurements of either kind and we discarded them manually.

After completion of the five steps defined in the first paragraph, we use RDS/TOP7 measurements to produce averaged values at the beginning of each hour on every sol, and at each half of the hour on every two sols. In each case, the averaging period is five minutes. This strategy nominally results in 36 sub-hourly values per sol: 24 at the beginning of each hour and 12 at every half of the hour. For consistency, we apply the same averaging method to every MEDA observed or derived quantity used in this article.

3.1.1.2. Upwelling Flux Reflected by the Surface: TIRS/IR3

The most processed TIRS/IR3 dataset available in the PDS is 'Calibrated Data' (*CAL_TIRS* files), which provides values of the reflected solar flux in the 0.3–3 μm band for a hemispherical FoV (Sebastián et al., 2020; 2021). To calculate SW_u, we convert these fluxes to 0.2–5 μm by using a look-up table generated by our COMIMART model (ds02 in SI).

In the *CAL_TIRS* measurements, there are associated flags indicating whether there are shadows cast by the RSM or the rover body in the FoV of the TIRS downward-looking channels (IR3–5; Table 1). In this work we keep track of this flag to account for the existence or lack of shadows among all TIRS/IR3 measurements.

3.1.2. Longwave Flux

TIRS measures LW_d and LW_u in the 6.5–30 μm range (Table 1). As required in quantifications of the radiative and surface energy budget, we explain next how we extend these measurements to the entire longwave range (5–80 μm).

3.1.2.1. Downwelling Atmospheric Flux: TIRS/IR1

LW_d values in the 6.5–30 μm range are available in the PDS as 'Calibrated Data' (*CAL_TIRS* files), while extended LW_d values in the 5–80 μm range are available as 'Derived Data' (*DER_TIRS* files). Therefore, 'DER' files contain the highest-order products for TIRS/IR1.

Following in-flight recalibrations and improved procedures developed during the first year of operations of Perseverance, updated 'DER' LW_d values will be first made available in the PDS on November 21, 2022, and will cover the first 539 sols of the mission. We show these updated values in this article for the first 350 sols (L_s ~ 6°–174° in MY 36). Therefore, PDS users should ignore 'DER' LW_d values made available in the PDS prior to November 21, 2022.

The main complexity in converting LW_d values from 6.5–30 μm to 5–80 μm is that the emission spectrum of the atmosphere cannot be accurately approximated to that of a blackbody. Instead, it is mainly determined by the strong emission of CO_2 at 15 μm (IR2), and the dust emission spectrum across the LW range. Following these considerations, we use 'CAL' LW_d values, IR2 measurements of temperature and irradiance in the 14.5–15.5 μm range, and the spectral responses of IR1 and IR2 (Sebastian et al., 2020) to convert 'CAL' to 'DER' LW_d values. From these three datasets, the temporal evolution of the ratio between the radiative fluxes measured by the IR1 and IR2 channels is calculated and compared to that simulated with the University of Helsinki/Finnish Meteorological Institute Single Column Model (hereinafter called SCM) for different values of aerosol optical depth model (Savijärvi et al., 2021). Following this comparison, an estimate of the diurnal evolution of atmospheric aerosol opacity is obtained. Then, we use observations of the atmospheric spectra in the 5–29 μm range measured by Mini-TES for different aerosol opacities and atmospheric temperature profiles (Smith et al., 2006) to obtain a linear function, which is used to convert 'CAL' into 'DER' LW_d values as a function of opacity and measured atmospheric temperature. Finally, we convert radiance measured at a fixed elevation angle (+35°; Table 1) to that corresponding to a hemispherical FoV by using the diffusivity-factor approximation (Elsasser, 1942). This methodology will be presented in a standalone article, which is currently in preparation.

Both in the 'CAL_TIRS' and 'DER_TIRS' files, there is a flag indicating whether the Sun is in the FoV of the upward-looking channels IR1 and IR2. We discard these measurements, as they result in values that are unrealistically high. Additionally, TIRS has performed several in-flight recalibrations during the first 350 sols of the mission, during which 'CAL_TIRS' and 'DER_TIRS' measurements are affected by controlled, artificial heating of the thermal plate. We discard these measurements too. The complete list of sols and LMST when these recalibrations were performed is available in the SI (ds03).

3.1.2.2. Upwelling Flux Emitted by the Surface: TIRS/IR4

LW_u values in the 6.5–30 μm range are available in the PDS as 'Calibrated Data' (*CAL_TIRS* files), while extended LW_u values in the 5–80 μm range are available as 'Derived Data' (*DER_TIRS* files).

To convert 'CAL' to 'DER' LW_u values, we took the following steps: (1) derivation of an equivalent surface brightness temperature for the ground (T_{b_IR4}) using 'CAL' LW_u measurements, the calibration equations obtained during pre-flight calibrations (Sebastián et al., 2020; 2021), and the blackbody assumption for the ground (surface unit emissivity, ε), and (2) calculation of LW_u in the 5–80 μm range by using Stefan-Boltzmann emission law as $LW_u = \sigma \times T_{b\_IR4}^4$, where $\sigma = 5.67\times10^{-8}$ W m^{-2} K^{-4} is the Stefan Boltzmann constant.

This methodology represents a simplification because the surface spectral emissivity, $\varepsilon(\lambda)$, varies across the 5–80 μm range, as observed by Mini-TES in the ~7–25 μm range, (Hamilton et al., 2014). To quantify the error in assuming unit emissivity, we have performed sensitivity studies using $\varepsilon(\lambda)$ values measured by Mini-TES. Results of this analysis yield relative errors in 'DER' LW_u values of up to 3% for equivalent surface brightness temperature of ~290 K, and up to 6% for equivalent surface brightness temperature of ~180 K.

Similar to SW_u, there are flags in the 'CAL' and 'DER' files indicating whether there are shadows in the FoV of TIRS/IR4. Here, we consider all measurements, accounting for the existence or lack of shadows by keeping track of this flag. As for LW_d, we discard measurements taken during in-flight recalibration activities (ds03 in SI).

3.1.3. Turbulent and Latent Heat Flux

The turbulent or sensible heat flux is defined as $H_0 = \rho c_p (\overline{w'T'})_s$, where ρ is the air density, c_p = 736 J Kg^{-1} K^{-1} is the specific heat of CO_2 gas at constant pressure, and $(\overline{w'T'})_s$ is the kinematic heat flux, defined as the covariance between the turbulent departures of air temperature, T', and vertical wind speed, w'. The symbol "s" stands for near-surface heights in which the kinematic heat flux is constant, while the overbar denotes an averaging period of a few minutes such that departures from the mean in temperature and vertical wind speed fall within the turbulent spectral range (e.g., Banfield et al., 2020).

While turbulent departures in temperature can be analyzed using measurements from the ATS (Munguira et al., 2022; de la Torre-Juarez et al., 2022; this issue;) and SuperCam microphone (Chide et al., 2022; this issue), neither the vertical wind speed nor its turbulent departure can be accurately obtained by the WS. This is why these values are 'blank' in the PDS. Therefore, we use Monin-Obukhov similarity theory to calculate H_0 as:

$$H_0 = k^2 U_a \rho_a c_p f(R_B) \frac{(T_g - T_a)}{ln^2(z_a/z_0)}, \quad (2)$$

where k = 0.4 is the Von Karman constant, U_a is the horizontal wind speed measured by the WS, $\rho_a = P/(RT_a)$ is the air density derived from PS and ATS measurements, with R = 191 J Kg^{-1} K^{-1} the Martian gas constant, z_a = 1.45 is the height of the ATS and WS, z_0 is the surface roughness (set to 1 cm; Hébrard et al., 2012), and $f(R_B)$ is a function of the bulk Richardson number $R_B = \frac{g}{T_g}\frac{(T_a - T_g)z_a}{U_a^2}$ defined as $f(R_B) = (1 - 40R_B)^{1/3}$ if $T_g > T_a$, and $f(R_B) = \max(0.007, \frac{1}{(1+5R_B+40R_B^2)^2})$ if $T_g < T_a$. This function accounts for the thermal stability in the first 1.45 m, and it has been tested under Earth Polar conditions (Savijärvi & Määttänen, 2010), which are a reasonable environmental Mars analogue.

The latent heat flux is defined as $L_f = \rho_a L_v (\overline{w'q'})_s$, where $L_v = 2.8 \times 10^6$ J/Kg is the latent heat of sublimation for water vapor, and q' is the turbulent departure of specific humidity. As for H_0, L_f has not been measured on Mars due to the lack of measurements of w' and q'. Nonetheless, this flux can be estimated using similarity theory and available measurements (see Eq. (7) in Martínez et al., 2021). Due to the extremely low specific humidity values (Fig. 3h) at the times

when frost might have formed at Jezero (Polkko et al., 2022; this issue), L_f values are of the order of a few tenths of W/m^2 or less, and thus can be neglected compared to the other terms of the SEB.

3.1.4. Net Heat Flux

The net heat flux into the ground is obtained from Eq. (1), where all the terms on the right-hand side are calculated as explained in previous subsections. We note that fluxes in Eq. (1) are referenced to a horizontal surface; however, fluxes measured by MEDA are referenced to Perseverance's local frame, the origin of which is located between the rover middle wheels and moves with the rover. In this local frame, +X is along the local north direction, +Z is along the downward normal at the landing site, and +Y completes the right-hand frame.

Using measurements of the rover's roll and pitch available in the PDS as 'Ancillary Data' (*DER_ANCILLARY* files), the inclination of the terrain traversed by the rover can be calculated as $\sqrt{(roll^2 + pitch^2)}$ (Fig. S4). However, this inclination is not necessarily the same as that of the terrain seen by the downward-looking TIRS channels (Fig. 2), which is not known. For this reason, we do not attempt to correct measured fluxes for the inclination, and we simply assume that they are referenced to a horizontal frame. This is a reasonable approximation because between 10:00 and 14:00 LMST, when the solar flux is maximum, the ratio between fluxes referred to the local frame and a horizontal surface can be approximated by μ_{lf}/μ_h, where μ represents the cosine of *SZA*. Under this approximation, and given inclinations shown in Fig. S4, most of the relative differences between fluxes stay below 5%, although they can be as large as ~20% for extreme inclination values ~15°.

Since MEDA measurements of the SEB are novel, we assessed them by comparing each term of Eq. (1) with SCM-simulated values. We used SCM instead of COMIMART because while solar fluxes simulated by both models are nearly identical, only SCM can simulate LW fluxes. Fig. 4 shows the terms of the SEB on sol 30 obtained from MEDA (symbols) and simulated with SCM (solid lines). On this sol, and on any other during the first 350 sols of the mission, the agreement between measurements and simulations is very good for each term of the SEB except for LW_d (red), which is systematically overestimated by the model. This behavior and its implications are discussed in detail in Section 5.

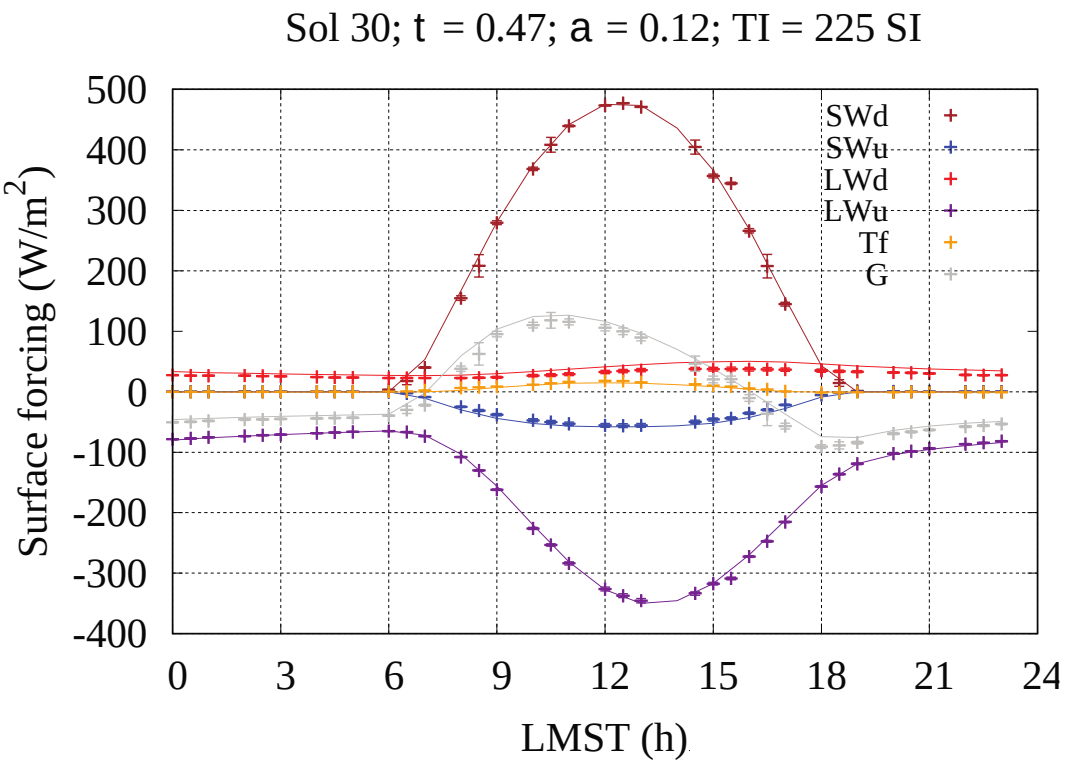

Figure 4. Surface energy budget on sol 30 (Ls ~ 20°) as a function of LMST obtained from MEDA (symbols) and simulated with SCM (solid lines). Colors represent the terms of the SEB in Eq. (1). Except for the downwelling LW flux (red), which is systematically overestimated by the model, there is a very good agreement between observations and simulations. This behavior repeats on every other sol. SCM was run on sol 30 using the following values: visible aerosol opacity, τ = 0.47 (obtained from Mastcam-Z, Fig. 3a), albedo at noon, α = 0.12 (obtained from MEDA), and thermal inertia, *TI* = 225 J m^{-2}K^{-1}s$^{-1/2}$, which provides the best SCM fit to measured ground temperatures).

3.2. Albedo

We determine the broadband hemispherical albedo (hereafter referred to as "albedo") in the 0.3–3 µm range as $\alpha = SW_u^{0.3-3\mu m}/SW_d^{0.3-3\mu m}$. Here, $SW_u^{0.3-3\mu m}$ is the reflected solar flux in the 0.3–3 µm band for a hemispherical FoV (available in the PDS as 'CAL' values), and $SW_d^{0.3-3\mu m}$ is the downwelling solar flux in the 0.3–3 µm band for a hemispherical FoV, which is obtained following the same five steps enumerated in the first paragraph of Subsection 3.1.1.1, except for extending RDS/TOP7 measurements from 0.19–1.2 to 0.3–3 µm (SI; ds02, fourth column). Based on uncertainties in measured solar fluxes, the relative error in albedo is < 10% in the vicinity of noon, and < 20% towards sunset and sunrise.

To obtain α when the RDS/TOP7 was saturated (around noon between sols ~270 and 350), we used COMIMART to simulate $SW_d^{0.3-3\mu m}$ with aerosol opacity values from Mastcam-Z. Prior to sol 270 (Ls ~131°), relative differences between $SW_d^{0.3-3\mu m}$ obtained from RDS/TOP7 and simulated by COMIMART are below 5% at LMSTs around noon, and therefore this is a reasonable approximation to calculate α in the absence of RDS/TOP7 measurements.

In order to analyze the illumination and viewing geometry, we use contemporaneous 'Ancillary' datafiles available in the PDS as 'Derived Data'. In addition to the roll and pitch, these files contain values of the *SZA*, the solar azimuth angle (ϕ_S) relative to the M2020 local frame (defined as the angle between the positive X-axis and the orthogonal projection of the Sun onto the XY plane, with +90° pointing West), and the rover's yaw (ϕ_R) relative to the M2020 local frame (defined as the counterclockwise rotation angle about the +Z-axis of the M2020 local level frame, with +90° pointing East).The dependence of the albedo on the illumination and viewing geometry is shown in Section 4.3.

3.3. Thermal Inertia

For each sol when the rover was parked, we obtained thermal inertia (*TI*) by solving the one-dimensional heat conduction equation for homogeneous terrains, Eq. (3). We used MEDA measurements of the surface energy budget as the upper boundary condition, Eq. (4), and a constant temperature T_d at a depth z_d as the lower boundary condition, Eq. (5).

$$\frac{\partial T(z,t)}{\partial t} = \left(\frac{TI}{\rho c}\right)^2 \frac{\partial^2 T(z,t)}{\partial z^2} \qquad (3)$$

$$-\left(\frac{TI}{\rho c}\right)\frac{\partial T(z=0,t)}{\partial z} = G = SW_d - SW_u + LW_d - LW_u - H_0 - L_f \qquad (4)$$

$$T(z = z_d, t) = T_d \qquad (5),$$

Here, ρ is the soil density, c the soil specific heat, and z_d is the diurnal penetration depth obtained as $z_d = 3 \times \sqrt{(2/\omega)}\left(\frac{TI}{\rho c}\right)$, where ω = 7.0774 × 10^{-5} s^{-1} is the angular speed of the planet's rotation and $L = \sqrt{(2/\omega)}\left(\frac{TI}{\rho c}\right)$ is the diurnal e-folding depth.

Assuming a fixed value of ρc = 1.2 × 10^6 J m^{-3} K^{-1}, *TI* and T_d are the only unknowns in Eqs. (3–5). By minimizing the difference between measured and numerically simulated values of the diurnal amplitude of ground temperature, the solution to Eqs. (3–5) is unique. This is because while higher (lower) T_d values shift the solution T(z = 0,t) towards higher (lower) values, *TI* controls the diurnal amplitude (e.g., Martínez et al., 2014). Thus, there is only one pair of *TI* and T_d values that satisfy our imposed condition simultaneously.

To evaluate the uncertainty in *TI*, we performed sensitivity studies in Eqs. (3–5) by varying the values of ρc between 0.8×10^6 and 1.6×10^6 J m^{-3} K^{-1} (Zent et al., 2010; Martínez et al., 2014; Grott et al., 2021; Piqueux et al., 2021), z_d between 2 × L and 4 × L, and G between its maximum and minimum values based on uncertainties of the various terms on the right-hand side of Eq.

(1). We obtained relative variations in *TI* of ~2% for the considered range of ρc and z_d, and ~8% for *G*. From these, we obtain an upper limit for the relative error in *TI* of ~10%.

To validate our methodology to obtain *TI*, we show in Fig. 5 the ground temperature as a function of LMST on sol 30 (Ls ~ 20°) measured by TIRS (black) and numerically solved from Eqs. (3–5) with a best-fitting value of *TI* = 215 SI units (red). The agreement is very good except for a cool bias in the numerical values (red) during early and late daytime hours. A similar behavior is found on other sols. This cool bias is explained by the assumption of homogeneous terrains, which we take in this study for the sake of simplicity and to obtain *TI* values without the need for models. The reader is referred to Savijärvi et al. (2022; this issue) for further discussions of the heterogeneity of the terrain across Perseverance's traverse and its impact on the determination of thermal inertia.

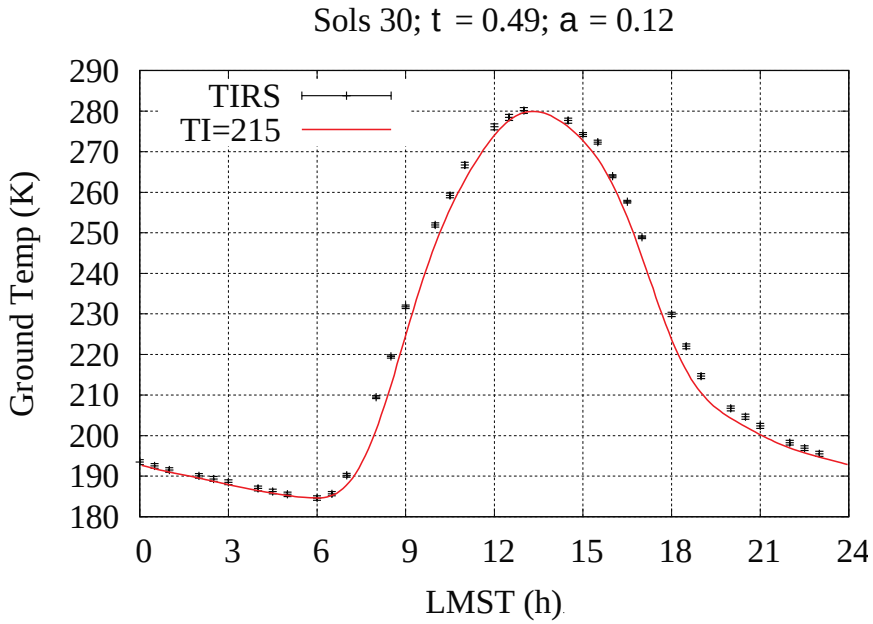

Figure 5. Ground temperature as a function of LMST on sol 30 (Ls ~ 20°) measured by TIRS (black) and solved numerically from Eqs. (3–5) with a best-fitting value of *TI* = 215 SI units. The cool bias in the numerical values during early and late daytime hours is caused by the assumption of a homogeneous terrain, which we take in this study for the sake of simplicity. Note that the best-fitting value of *TI* obtained by SCM is 225 SI units (Fig. 4). A similar good match in *TI* between SCM and MEDA observations (Eqs. (3–5)) is obtained for other sols.

4. Results

We show results of thermal inertia in Section 4.1, which facilitate analyses of the surface energy budget presented in Section 4.2. Then, we show results of albedo in Section 4.3.

4.1. Thermal Inertia

Fig. 6 (left) shows *TI* values for those of the first 350 sols of the M2020 mission where the rover was parked for at least an entire sol. Depending on the type of terrain, *TI* values ranged from 180 SI units on sol 106 (Fig. 6, bottom right; sand dune) to 605 SI units on sol 125 (Fig. 6, top right; bedrock-dominated material). This range of variation is nearly identical to that at the MSL

landing site during the first 2500 sols of that mission, with values between 170–610 SI units (Hamilton et al., 2014; Vasavada et al., 2017; Martínez et al., 2021).

TI values varied less than ~8% when the rover was parked in the same location for multiple sols (e.g., sols 138–152, 181–199, 211–237, or 249–276), consistent with the 10% relative error estimated for *TI*. An exception to this occurred during sols 287–328 (Ls ~140°–161°), coinciding with the local dust storm on sols 312–318 (Ls 152°–156°). During this period, *TI* increased from an averaged value of 290 SI units on sols 287–312 to 315 SI units on sols 313–328 (Fig. 6, left). Although this difference (25 SI units) is at the limit of the estimated uncertainty, *TI* values were repeatedly lower before the dust storm and repeatedly higher during and after. This suggests that the dust removal and sand transport which occurred on the FoV of TIRS during the dust storm (Vicente-Retortillo et al., 2022; this issue) might explain this behavior, as a terrain with less dust would present higher TI values. In future work, we plan to evaluate the thickness of dust layer consistent with the decrease in *TI*, and whether that thickness is realistic given the dust budget at the surface of Jezero.

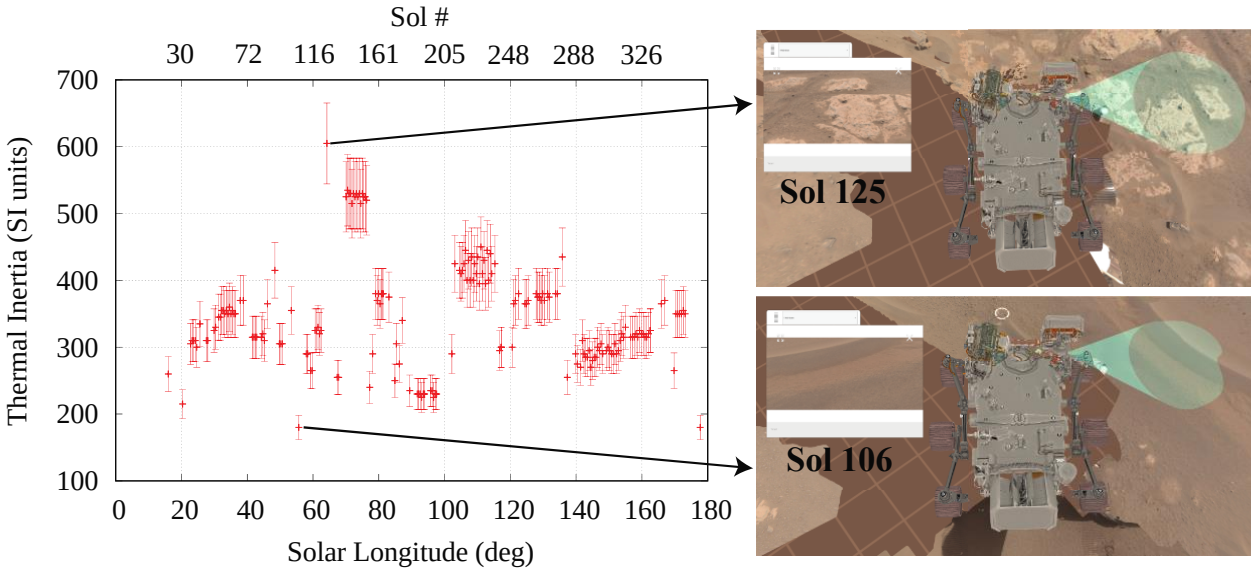

Figure 6. (**Left**) Thermal inertia values for the first 350 sols of the M2020 mission when the rover was parked for an entire sol. (**Right**) FoV of TIRS downward-looking channels (green shaded, ellipsoidal area of ~3–4 m^2) on sols 125 (top) and 106 (bottom), corresponding to the terrains with the lowest (sand dune) and highest (bedrock-dominated material) *TI* values.

As expected, terrains with higher (lower) values of *TI* underwent smaller (larger) diurnal amplitudes of ground temperature, ΔT_g (Fig. 3c) For instance, the relatively low *TI* (230 SI units) on sols 181–199 (Ls in 90°–97°) resulted in relatively large ΔT_g ~ 87 K, while the relatively high *TI* (525 SI units) on sols 138–152 (Ls in 70°–76°) resulted in relatively low ΔT_g ~ 56 K.

Fig. 7 shows a thermal inertia map with values derived from MEDA (circles) and retrieved from the Thermal Emission Imaging System (THEMIS) on board the Mars Odyssey spacecraft (squares). Given THEMIS' spatial resolution of 100 m per pixel (Fergason et al., 2006), we obtained THEMIS *TI* values as the average over 0.001° × 0.001° lon/lat boxes of three collocated

stamps ('I02413002', 'I36033008', and 'I45156005') queried with the JMARS software and processed with the MARSTHERM model to derive *TI* values as a function of longitude and latitude (Putzig et al., 2013; Putzig and Mellon, 2007; Mandon et al., 2022).

While THEMIS retrievals ranged between 295 and 350 SI units across Perseverance's traverse, MEDA-derived values ranged between 180 and 605 SI units. These departures are caused by the different spatial resolution between both datasets (~3–4 m^2 versus 10^4 m^2). Nonetheless, there is an overall good agreement between both datasets when *TI* averages over Perseverance's traverse are considered, with values of 350 SI units derived from MEDA, and 330 SI units derived from THEMIS.

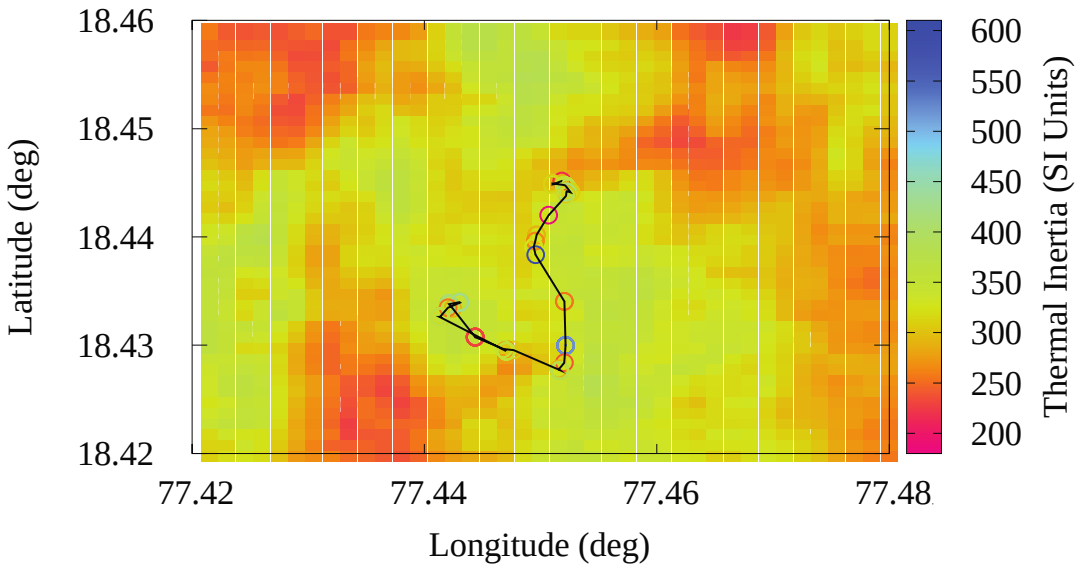

Figure 7. Color-coded thermal inertia map showing values retrieved from THEMIS (squares) and obtained from MEDA (circles). The black line represents the rover's traverse for the first 350 sols. While MEDA-derived *TI* values ranged between 180 and 605 SI units across Perseverance's traverse (black line), THEMIS retrievals range between 295 and 350 SI units. These departures are caused by the different spatial resolution of both datasets.

For *TI* values below ~350 SI units, the effective particle size of the surface can be estimated using an experimental relationship between the thermal inertia and the diameter (d) of homogeneous spheres (Presley and Christensen, 1997):

$$d(\mu m) = \left(\frac{TI^2}{\rho c \times C P^{0.6}}\right)^{1/-0.11\log(P/K)} \qquad (6).$$

Here, C = 0.0015 and K = 8.1 × 10^4 torr are empirically-derived constants, ρc = 1.2 × 10^6 J m^{-3} K^{-1}, and P is the atmospheric pressure in torr. Using Eq. (6), *TI* values from Fig. 6 (left), and P values from Fig. 3b (daily mean), we obtained particle sizes ranging from ~57 μm to almost 1 mm (Fig. S5). As future study, we plan to compare these values with particle sizes directly inferred from M2020 imagery, as well as to classify the geological type of terrain as a function of TI, albedo and grain size.

4.2. Surface Energy Budget

Figs. 8 and 9 show the seasonal and diurnal evolution of each term of the SEB, respectively. We discuss each term below.

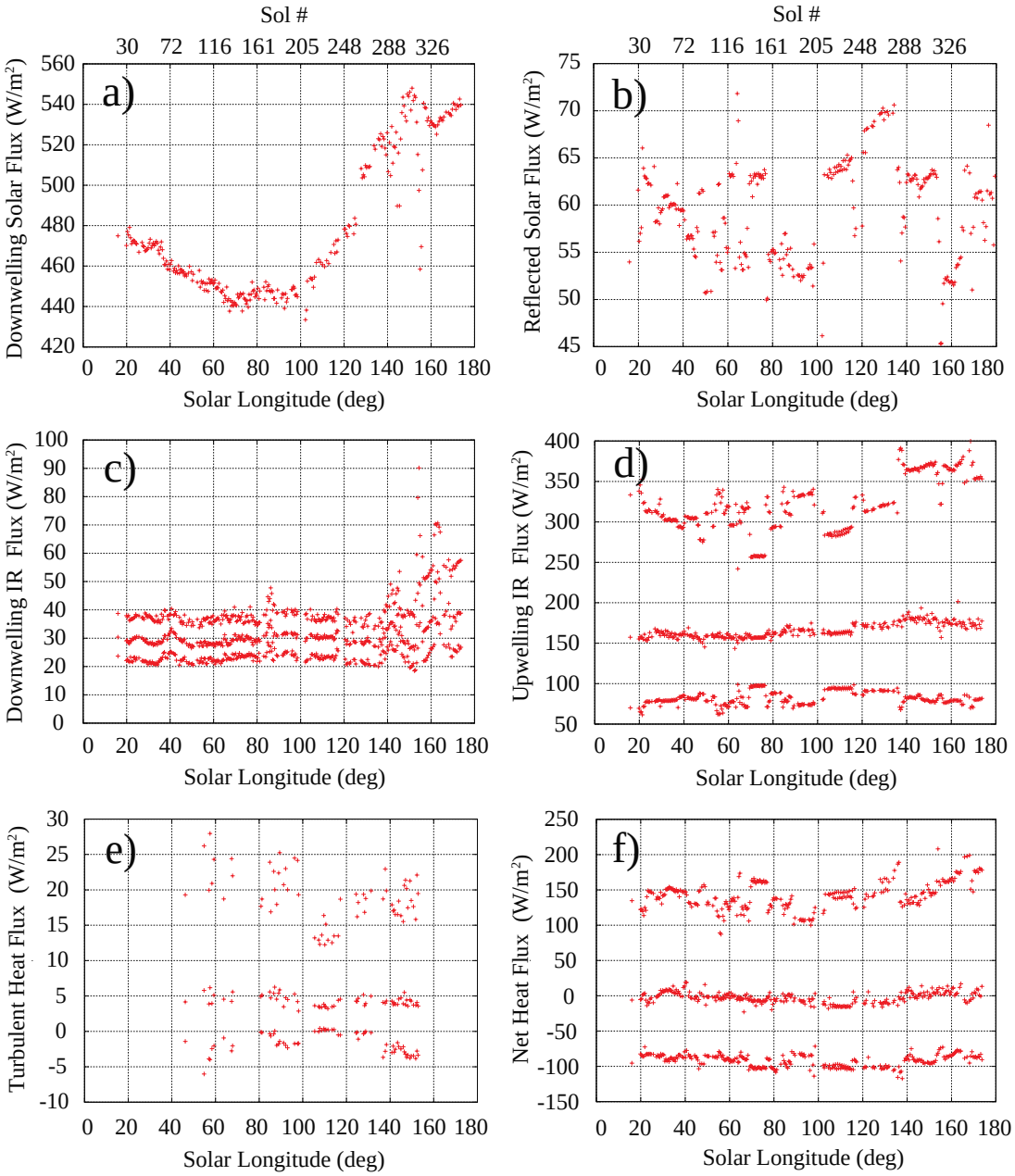

Figure 8. Surface energy budget at Jezero crater as a function of Ls during the first 350 sols of the Mars 2020 mission. **(a)** Daily maximum downwelling solar flux (SW_d; 0.19–5 μm). **(b)** Daily maximum reflected solar flux (SW_u; 0.19–5 μm). **(c)** Daily maximum, mean, and minimum downwelling longwave flux (LW_d; 5–80 μm). **(d)** Daily maximum, mean, and minimum upwelling longwave flux emitted by the surface (LW_u; 5–80 μm). **(e)** Daily maximum, mean, and minimum turbulent heat flux (H_0). **(f)** Daily maximum, mean, and minimum net heat flux into the ground (G).

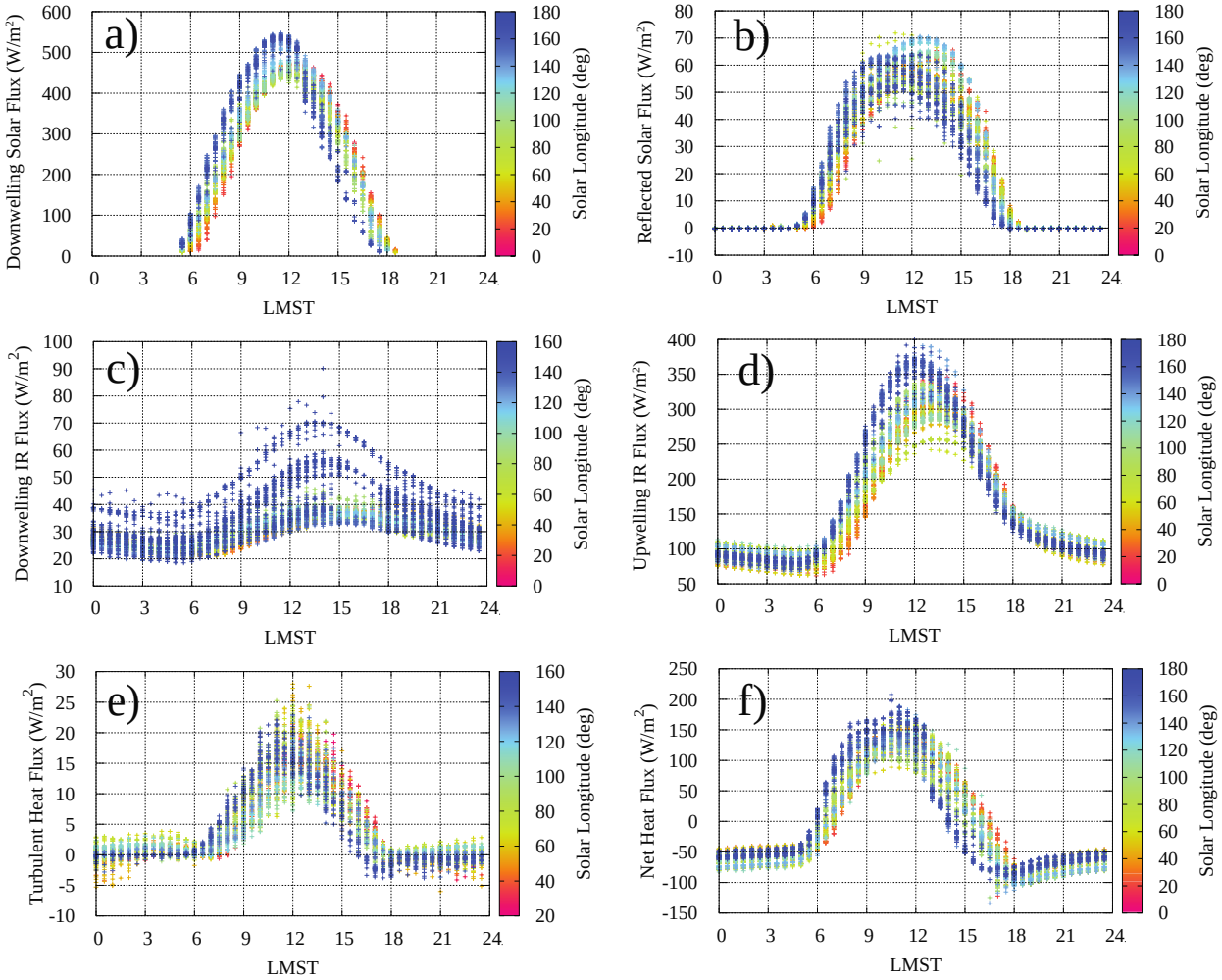

Figure 9. Diurnal evolution of the surface energy budget, Eq. (1), at Jezero crater for the first 350 sols of the Mars 2020 mission. Color-bar is used for Ls. Letters in each subpanel refer to the same term as in Fig. 8.

4.2.1. Shortwave Flux

The seasonal evolution of the daily maximum SW_d is shown in Fig. 8a. During the aphelion season, when the aerosol opacity is low and relatively stable (Fig. 3a), the seasonal evolution of SW_d is governed by the solar insolation at the top of the atmosphere (TOA; Fig. S6). In particular, SW_d showed a relative minimum at Ls ~65° (same as in the TOA) and an absolute maximum at Ls ~150°, when the aerosol opacity was relatively low (Fig. 3a). SW_d decreased significantly during the regional dust storm occurred on sols 312–318 (Ls 152°–156°), returning to pre-storm values immediately after as the aerosol opacity decreased (Lemmon et al., 2022). For comparison of SW_d with other landing sites, the reader is referred to Martínez et al. (2017).

The diurnal variation of SW_d is shown in Fig. 9a. Daily maximum SW_d values typically occurred between 12:00 and 12:30 LMST for Ls in 20°–80° (first 160 sols; red-green colors), and between 11:00 and 12:00 LMST for Ls in 80°–180° (sols 160–350; green-blue colors). In addition to

changes in the rover tilt and yaw, this behavior is mainly caused by differences between LMST and local true solar time (LTST), which range from around +30 minutes at the beginning of the mission to -40 minutes at Ls 180° (with LMST ≈ LTST at Ls = 57° on sol 110).

The seasonal and diurnal evolution of SW_u are shown in Figs. 8b and 9b, respectively. SW_u did not follow any particular trend in Ls, as it depends on the albedo of the terrain which changes along Perseverance's traverse. As for the diurnal variation, daily maximum SW_u values occurred between 10:00 and 14:00 LMST depending on the albedo and illumination and viewing geometry (more details in Section 4.3).

4.2.2. Longwave Flux

The daily maximum, mean and minimum LW_d are shown in Fig. 8c, with four relative maxima at Ls ~40° (sol 73), Ls ~86° (sol 174), Ls ~145° (sol 298), and Ls ~154° (sol 315; regional dust storm). To facilitate correlations with the opacity and thermal environment, Fig. 10 shows color-coded values of LW_d (top), aerosol opacities at 9 μm retrieved from TIRS IR1 and IR2 measurements with an uncertainty < 0.02 (middle; Smith et al., 2022), and air temperature at about 40 m (bottom) as a function of Ls and LMST. The black arrows mark the Ls for each of the four relative maxima in LW_d in Fig. 8c.

It follows from Fig. 10 (middle) that each of these maxima were caused by periods of enhanced opacity. Interestingly, while opacity values retrieved from Mastcam-Z peaked at Ls ~145° and ~154°, they did not show particularly high values at Ls ~40° and ~86° (Fig. 3a). This is because Mastcam-Z operates during daytime, with most retrievals performed between 09:00 and 18:00 (Fig. S2a) when the aerosol opacity is relatively low (Fig. 10 (middle)). Thus, the peaks in LW_d at Ls ~40° and ~86° occurred because opacity values stayed relatively high throughout those sols, with LMST periods of low opacity (purple and blue colors) narrower than in other surrounding Ls periods.

The diurnal variation of LW_d, which is the most complex among the SEB terms, is shown in Figs. 9c and 10 (top). Typically, the daily maximum LW_d occurred between 13:00 and 16:00, and the daily minimum between 04:00 and 06:00, roughly following the air temperature at ~40 m measured by TIRS/IR2 (Fig. 10, bottom). However, the diurnal variation of LW_d is more complex than that of T_a at 40 m, as it is also affected by aerosol opacity. As an example, Fig. 11 (top) shows the diurnal variation of LW_d and τ referenced at 9 μm for sols 288 and 289 (Ls ~ 140°). Not only does LW_d present significantly different values on both sols, but the LMSTs at which the daily maximum and minimum LW_d are achieved are also different. These departures are caused by the diurnal evolution of τ on both sols, with larger values and different LMST peaks on sol 298. However, the evolution of the air temperature at 40 m on both sols was nearly identical (Fig.11, bottom). This is because while LW_d and τ values are sensitive to the aerosol content and thermal profile in the entire atmospheric column, T_a values are determined by the thermal profile near the surface and are nearly insensitive to the aerosol content (Smith et al., 2022).

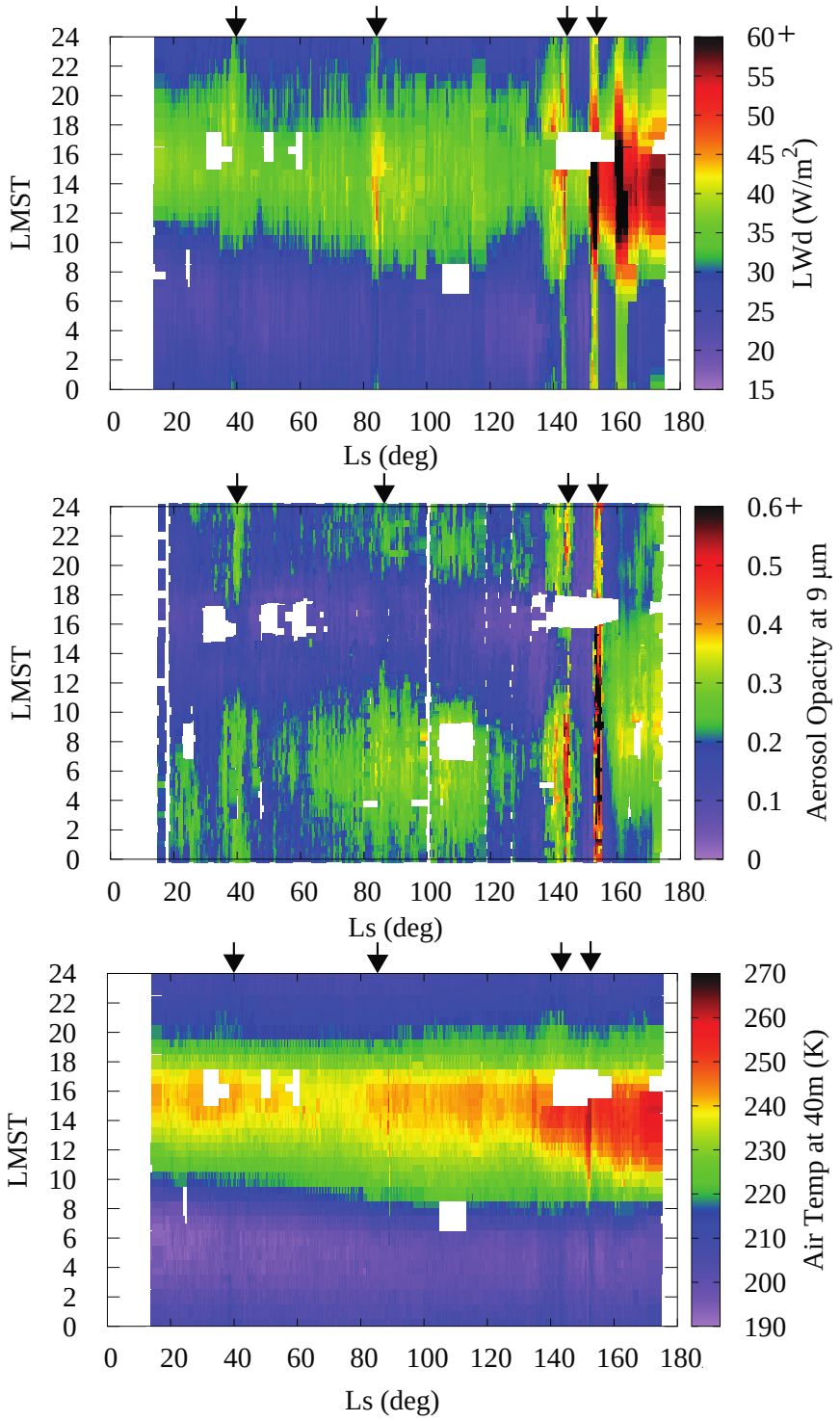

Figure 10. Color-coded downwelling LW flux (**top**), aerosol opacity at 9 µm (**middle**), and air temperature at ~40 m (**bottom**) as a function of Ls and LMST. The temporal gaps correspond to TIRS measurements taken either during in-flight calibrations or with the Sun within the FoV of IR1 and IR2. The black arrows mark the Ls at which the daily maximum, mean and minimum LW_d showed relative maxima (Fig. 8c).

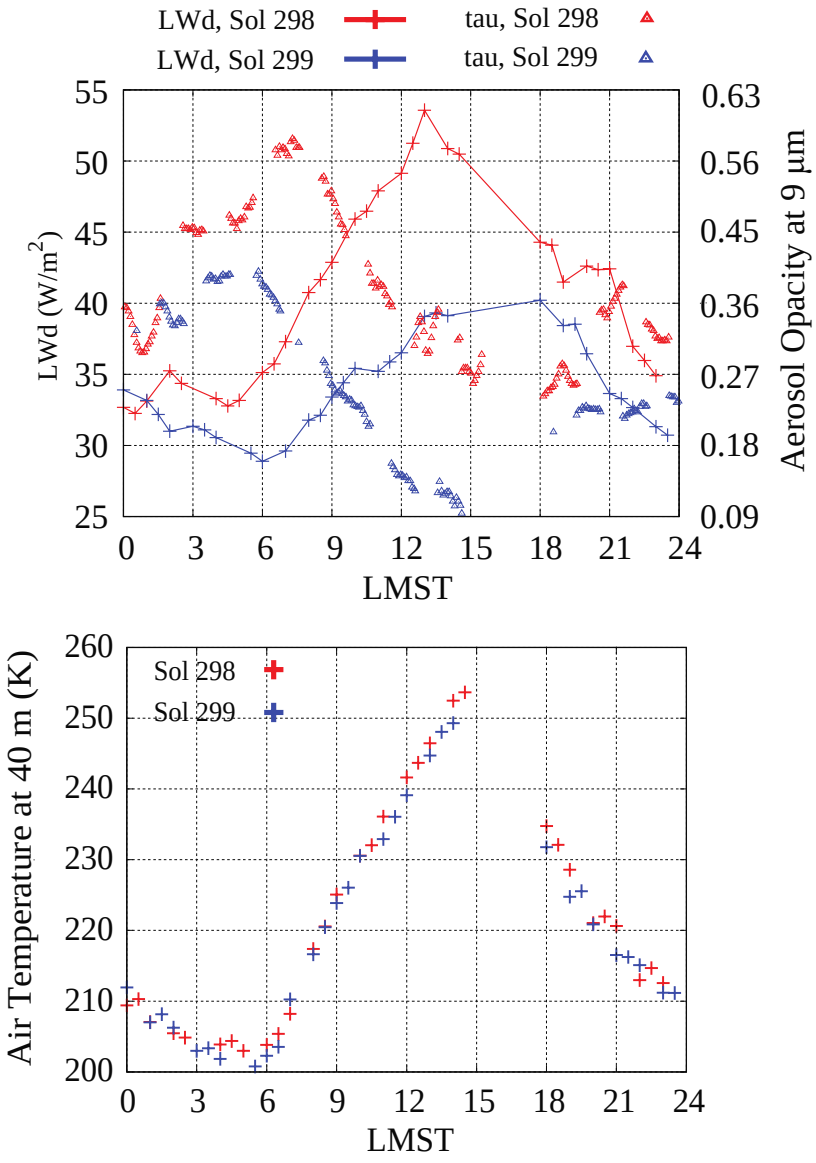

Figure 11. Diurnal evolution of the downwelling LW flux and aerosol opacity at 9 μm **(top)**, and the air temperature at ~40 m **(bottom)** on sols 288 (red) and 289 (blue). LW_d values are connected with a colored line for the sake of clarity. While LW_d fluxes and τ differ on both sols both quantitatively and qualitatively, the air temperature measured by TIRS/IR2 is similar. This is because TIRS/IR2 measurements are mainly determined by the thermal profile in the first few hundred of meters (with the largest contribution from air layers at ~40 m), whereas LW_d and τ are sensitive to the aerosol content and thermal profiles in the entire atmospheric column.

LW_d was indirectly estimated at Gale crater using *in-situ* measurements from the MSL/REMS instrument (Martínez et al., 2021). Between Ls 20° and 150°, daily mean values of LW_d ranged between 20 and 40 W/m^2 at Gale, in good agreement with values ~30 W/m^2 observed at Jezero (Fig. 8c). Between Ls 150° and 180°, the daily mean LW_d increased monotonically from 40 to 60 W/m^2 at Gale, while at Jezero it also showed an upward trend from 30 to 40 W/m^2 following

periods of enhanced opacity. As for the diurnal evolution, LW_d peaked between 15:00 and 16:00 LMST in the Ls 0–180° period at Gale, in good agreement with Jezero (Fig. 9c). A secondary LW_d peak was estimated at Gale between 06:00 and 09:00, which was likely attributed to inaccuracies in the estimation of LW_d (Fig. 9 in Martínez et al., 2021). This secondary peak has not systematically appeared at Jezero, although the diurnal evolution of LW_d and τ are complex, with strong sol-to-sol variability (Fig. 11).

The daily maximum, mean and minimum LW_u is shown in Fig. 8d. This quantity is a measure of the ground temperature (Fig. 3c; Section 3.1.2.2.), and therefore strongly depends on the geophysical properties of the terrain, as well as on the solar flux reaching the surface. In particular, sol-to-sol variations are primarily caused by changes in the thermal inertia of the terrain (Figs. 8d and Fig. 6, left), while the seasonal evolution of the daily mean LW_u mostly follows that of SW_d (Figs. 8d and 8a), with a weak relative minimum at Ls ~65° and a weak relative maximum at Ls ~150°. Fig. 9d shows the diurnal evolution of LW_u, with most of the daily maximum values occurring between 13:00 and 13:30 LMST for Ls in 20°–80° (first 160 sols; red-green colors), and between 12:00 and 13:00 LMST for Ls in 80°–180° (sols 160–350; green-blue colors). Based on differences between LMST and LTST ranging from +30 minutes at the beginning of the mission to -40 minutes at Ls 180°, most daily maximum values of LW_u and T_g occurred around 13:00 LTST.

4.2.3. Turbulent Heat Flux

Fig. 8e shows the daily maximum, mean and minimum H_0 on sols with complete diurnal WS coverage (Fig. S1). Due to the thin Martian air ($\rho_a \sim 10^{-2}$ kg/m^3; Fig. 3f), H_0 shows the lowest maximum values among the SEB terms (excluding L_f). The strong sol-to-sol variability in the daily maximum and minimum H_0 is primarily caused by changes in the thermal gradient in the first 1.45 m (Eq. 2), which in turn is driven by changes in the thermal inertia of the terrain, and, to a lesser extent, in the aerosol opacity content. For instance, daily maximum H_0 values are lowest between Ls ~100° and 120° (sols 211–237), when the rover was parked on a terrain with relatively high thermal inertia (Fig. 6, left), and therefore relatively low thermal gradients in the first 1.45 m. Except for this long Ls period of relatively high *TI*, there seems to be a decreasing trend in H_0 from Ls to 60° to 145° (Fig. 8e), which was likely caused by the contemporaneous decrease in atmospheric density, as wind speeds did not show a marked seasonal variation (Fig. 3f; Eq. (2)). A similar Ls-dependence was found at the landing site of the MSL mission, where H_0 presented highest seasonal values when the air density was highest (Martínez et al., 2021). It is unclear if a similar decreasing trend with L_S is also found in the vortex and dust devil activity observed by MEDA (Hueso et al., 2022).

The diurnal variation of H_0 is shown in Fig. 9e, with positive values when $T_g > T_a$ and negative values when $T_g < T_a$ (Eq. (2)). Positive values correspond to convective conditions (H_0 directed from the surface to the atmosphere to cool down the surface), while negative values correspond to thermal inversions (H_0 directed from the atmosphere towards the surface to warm it up). Typically, the daily maximum H_0 occurred between 11:00 and 13:00 LMST, and the daily minimum occurred throughout 18:00 and 06:00, following in both cases the diurnal trend of T_g-T_a (Fig. 12, top). On some sols, T_g did not fall below T_a overnight and thus H_0 stayed positive throughout the sol (Fig. 12, top and Fig. 9e). This lack of local thermal inversion mostly occurred on terrains with *TI* > 390 SI units (Fig. 12, bottom), which corresponded to localized terrains

with *TI* values higher than the mean values across Perseverance's traverse obtained from MEDA (350 SI units) or THEMIS (330 SI units) (Section 4.1).

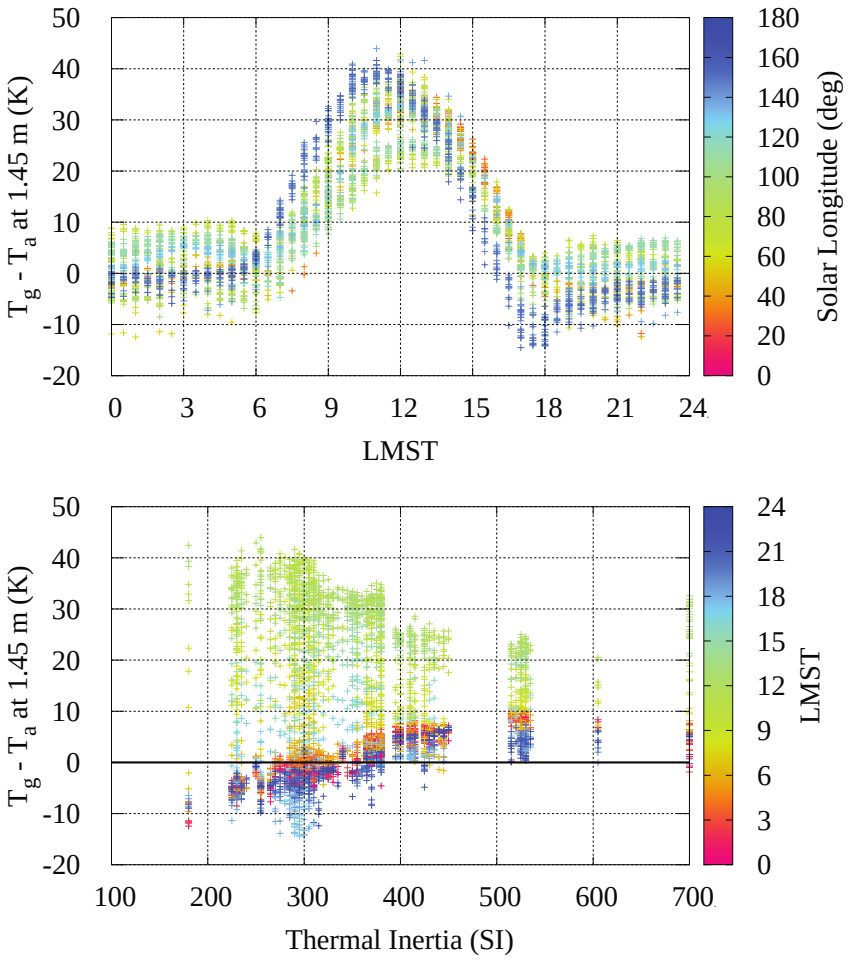

Figure 12. (**Top**) Diurnal evolution of the thermal gradient in the first 1.45 m as a function of LMST, with color code for Ls. This evolution governs the diurnal variation of the turbulent heat flux shown in Fig. 9e. (**Bottom**) Thermal gradient in the first 1.45 m as a function of thermal inertia, with color code for LMST. For *TI* > 390 SI units, the ground temperature generally stayed warmer than the air at 1.45 m throughout the night (horizontal black line), indicating a lack of local thermal inversion.

4.2.4. Net Heat Flux into the Ground

The daily maximum, mean and minimum net heat flux into the ground is shown in Fig. 8f. The coverage for this term is better than for H_0 because on sols without complete diurnal WS coverage, we obtained *G* from Eq. (1) by calculating H_0 values as the seasonal hourly average over the Ls 46°–152° (sols 85 and 313) period. This is a reasonable approximation given the lack of marked seasonal trend and low values of H_0 during this period.

In the absence of abrupt changes in aerosol opacity (and thus in SW_d and LW_d), the strong sol-to-sol variability in the daily maximum and minimum *G* (Fig. 8f) was primarily caused by changes

in thermal inertia and thus in LW_u via T_g (Figs. 3c, 6 left, and 8d). In particular, larger diurnal amplitudes in *G* typically resulted in higher *TI* values (Fig. S7).

Fig. 9f shows the diurnal variation of *G*. Positive values indicate heat conduction from the surface to the subsurface, while negative values indicate the reverse. For Ls in 20°–80° (red-green colors), positive values typically occurred between ~07:00 and ~15:00 LMST, with daily maximum values at ~11:00 LMST. For Ls in 80°–180° (green-blue colors), positive values occurred between ~06:00 and 14:00 LMST, with daily maximum values at ~10:30 LMST. On the other hand, negative values typically peaked between 18:00 and 19:00 LMST for Ls in 20°–80°, and between 17:00 and 18:00 LMST for Ls in 80°–180°. This shift in Ls was mostly caused by differences between LMST and LTST. By comparing the diurnal variations of *G* (Fig. 9f) and T_g (Fig. S2c), the daily maximum G typically occurred around 2 and 2.5 hours prior to the peak in T_g.

4.3. Albedo

Fig. 13 (top) shows the whole set of MEDA-derived broadband (0.3–3 μm) albedo values as a function of LMST during the Ls period in which the RDS/TOP7 was not saturated (first 270 sols). Only values with $SZA < 60°$ are shown to avoid large uncertainties close to sunrise and sunset. The two color-coded lines represent the albedo variation on sols 125 (Ls ~ 64°) and 209 (Ls ~ 102°), corresponding to the highest and lowest near-noon values during the first 270 sols. Fig. S8 shows TIRS' FoV on these two sols.

The albedo presented a marked non-Lambertian behavior on every sol, with lowest values occurring near noon and highest toward sunrise and sunset. This is a common observation in Earth deserts (e.g. Zhang et al., 2014) and has been observed from *in-situ* observations by the Viking and Mars Pathfinder landers (Guinness et al., 1997; Johnson et al., 1999) the Mars Exploration Rovers (Johnson et al., 2006a,b, 2021), and MSL (Johnson et al., 2022). To analyze the albedo as a function of the illumination and viewing geometry, we calculated values of the phase angle, β, defined as the angle between the incidence and emission vectors (Fig. S9; Shepard, 2017):

$$\cos\beta = \cos(SZA)\cos(e) + \sin(SZA)\sin(e)\cos(\Delta\phi). \quad (7)$$

In Eq. (7), *SZA* is the solar zenith angle, *e* is the emission angle between the surface normal and a vector to the observer (= 55° given the -35° pointing angle of TIRS/IR3; Table 1), and $\Delta\phi = |\phi_S - \phi_{TIRS}| + 180°$ is the difference between the solar azimuth angle, ϕ_S, and the TIRS' azimuth angle, ϕ_{TIRS}. This last angle is calculated from the rover's yaw, ϕ_R, as $\phi_{TIRS} = -\phi_R - 75°$ by accounting for the opposite local frames used in the definition of ϕ_S and ϕ_R in the PDS, and the 75° of separation clockwise between the rover forward direction and TIRS (Section 3.2 and Fig. 2). Low β values represent geometries when the Sun is directly behind TIRS' FoV, which occur when TIRS is pointing towards East or West and SZA ~ 55°. To illustrate this geometry, Fig. S10 shows the diurnal evolution of the various angles involved in Eq. (7) on sol 237, when the TIRS' FoV pointed approximately towards the East ($\phi_{TIRS} = -102°$).

Fig. 13 (middle) shows the albedo as a function of the phase angle, with *SZA* represented using the color code. The highest albedo values correspond to low phase angles because of the overall

backscattering nature of the Martian surface and the onset at smaller phase angles of the opposition effect. This occurs on surfaces when the Sun is directly behind the observer, and thus the shadows cast by their roughness elements (e.g., pores, pits) are minimized. The wider distribution of data points at the lowest phase angles likely represents variable inclusion of the rover mast's shadow in the TIRS' FoV. The upturn in the phase curves at $\beta > 70°$ demonstrates the forward scattering nature of some surfaces at high phase angles. Future work will analyze individual phase angle curves as a function of the number and size of the scatterers in the TIRS' FoV (as determined by Mastcam-Z and/or Navcam images).

Fig. 13 (bottom) shows the Ls evolution of the daily minimum α for the first 350 sols of the mission, which ranged from 0.159 on sol 125 (Ls ~ 64°) to 0.093 on sol 318 (Ls ~ 156°). The daily minimum albedo varied less than 5% on sols when the rover was parked, consistent with an estimated relative error < 10% (e.g., sols 138–152 and Ls 70°–76°; sols 181–199 and Ls 90°–98°; or sols 211–237 and Ls 103°–115°). As for thermal inertia, an exception to this occurred during the 140°–161° Ls period (sols 287–328), which included the local dust storm on sols 312–318 (Ls 152°–156°). From the beginning of this period to the onset of the storm, near-noon albedo values decreased from around 0.120 ± 0.007 to 0.110 ± 0.007. Then, during the storm, the albedo decreased to the lowest recorded values (0.093 ±0.006), and it remained approximately constant until sol 328 (Ls ~161°), when the rover drove. The reader is referred to Vicente-Retortillo et al. (2022; this issue) for a detailed study of the decrease in albedo during the regional dust storm, which was found to be caused by dust removal and sand transport, and to Lemmon et al. (2022; this issue) for a detailed study of the environmental conditions during this storm.

Comparisons among albedo values retrieved *in-situ* at different landing sites are problematic not only due to differences in the terrain, but also in the technique used to obtain the albedo, the available LTSTs at which observations were acquired, and the general assumption of the Lambertian approximation in previous studies. Rice et al. (2018) derived a range of Pancam-derived Lambertian albedos (0.4–1.0 μm) of 0.11–0.22 at Meridiani Planum (Opportunity, MER-B), and of 0.14–0.24 at Gusev crater (Spirit, MER-A), with most of these observations acquired within one hour from local noon. Using numerical modeling and ground temperature measurements, Vasavada et al. (2017) and Martínez et al. (2021) estimated Lambertian albedo values in the 0.06–0.28 range during the first 2500 sols of the MSL mission. Using a similar technique, Piqueux et al. (2021) estimated a Lambertian albedo of 0.16 at the InSight landing site.

Bolometric albedos in the 0.25–2.9 μm range have been retrieved from orbit by the Thermal Emission Spectrometer (TES) at around 14:00 LTST with a spatial resolution of ~300 km^2 and an uncertainty of 0.001. Fig. 14 shows a map of MEDA-derived albedo values at ~14:00 LMST (colored circles), with a greenish background color corresponding to a collocated TES-retrieved value of 0.147. While MEDA-derived values varied between ~0.10 and 0.18 depending on the location, the averaged value across Perseverance's traverse is 0.14, in very good agreement with TES. Comparisons with bolometric albedos in the 0.25-2.9 μm range retrieved from OMEGA with a spatial resolution between 1 and 2 km (Vincendon et al., 2015) are the subject of ongoing investigations.

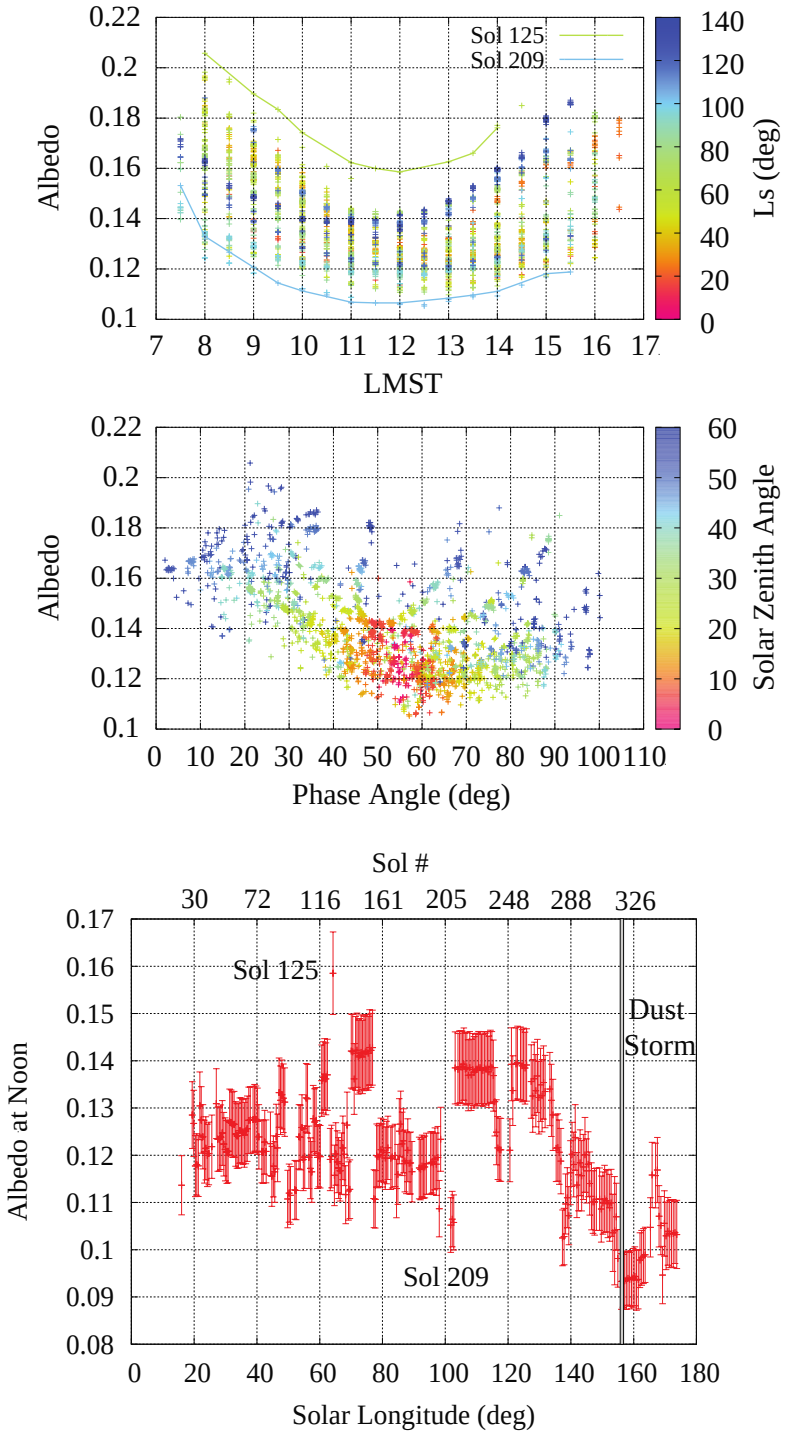

Figure 13. (**Top**) Diurnal variation of broadband (0.3–3 μm) albedo for the first 270 sols of the mission, corresponding to color-coded Ls values between 6° and 140°. The two color-coded lines represent the albedo on sols 125 (Ls ~ 64°) and 209 (Ls ~ 102°), when the highest and lowest near-noon values were observed. (**Middle**) Albedo as a function of phase angle and color-coded *SZA*. The brightest region corresponds to low phase angles. (**Bottom**) Daily minimum (near-noon) α as a function of Ls for the first 350 sols of the mission.

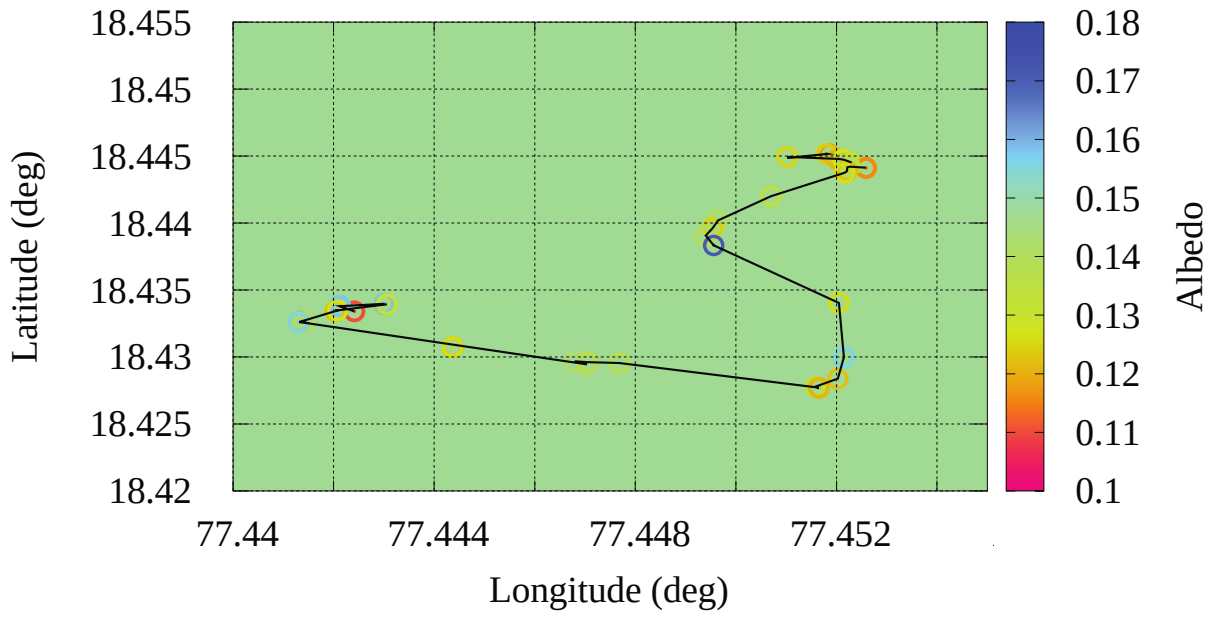

Figure 14. Color-coded albedo map showing MEDA-derived values at ~14:00 LMST (circles) across Perseverance's traverse (black line), and a TES-retrieved value of 0.147 (greenish background color) for the shown area at around the same local time. Although MEDA-derived values ranged between 0.1 and 0.18 depending on the terrain, the averaged MEDA-derived value across Perseverance's traverse is 0.14, in good agreement with TES.

5. Discussion: Atmospheric IR Flux

The agreement between MEDA observations and SCM simulations of each term of the SEB is quite good except for LW_d (Fig. 4), which is systematically and significantly overestimated by SCM. To illustrate this behavior, Fig. 15 shows the diurnal evolution of LW_d on sol 140 (Ls ~ 71°) observed by MEDA (red symbols) and simulated with SCM (solid black line). Also shown is the opacity retrieved from TIRS measurements (orange symbols; Smith et al., 2022), and retrieved from Mastcam-Z at ~17:22 LTST (solid orange line). Note that TIRS-derived opacity values have been obtained at 9 μm, but they are referenced here at 0.88 μm by multiplying them by a factor of 1.8.

Discrepancies between observed and simulated LW_d values might be explained by the assumption made in models (e.g., SCM) that aerosol opacity remains constant throughout the sol. While LW_d values simulated with SCM were obtained assuming a constant value of opacity given by Mastcam-Z, LW_d values observed by MEDA were retrieved in an environment with diurnally varying opacity values. As future work, we plan to analyze the impact of diurnally varying opacity on thermal profiles (and thus on LW_d) at diurnal and seasonal timescales, and in particular on temperature profiles measured by MEDA between the surface and about 40 m.

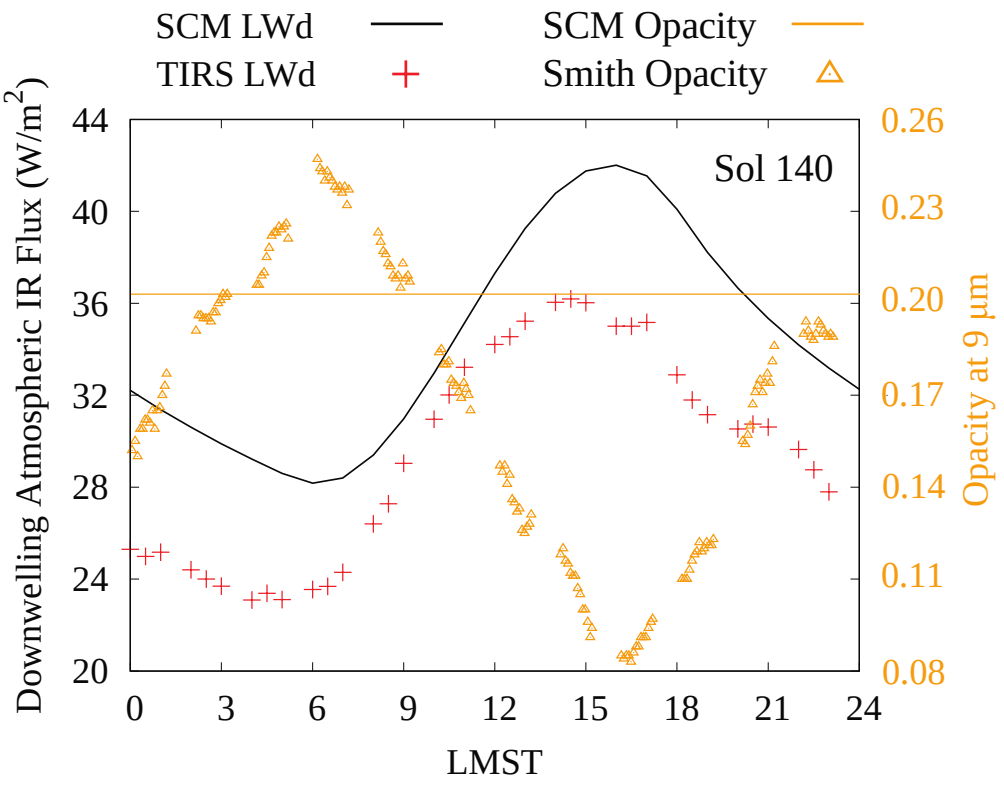

Figure 15. Diurnal evolution of the downwelling atmospheric IR flux observed by MEDA (red symbols) and simulated with SCM (black solid line) on sol 140 (Ls ~ 71°). The secondary Y-axis represents the aerosol opacity at 0.88 µm retrieved from TIRS (orange symbols), and retrieved from Mastcam-Z at ~17:22 LTST (solid orange line). SCM-simulated LW_d values were obtained assuming a constant opacity given by Mastcam-Z, while MEDA-observed LW_d values were retrieved in an environment with diurnally varying opacity.

6. Summary and Conclusions

MEDA allows the determination of the surface radiative budget on Mars for the first time through measurements of the incident and reflected solar flux, the downwelling atmospheric IR flux, and the upwelling IR flux emitted by the surface. Moreover, MEDA allows the calculation of the broadband (0.3–3 µm) albedo through measurements of the incident and reflected solar flux for a variety of illumination and viewing geometries. This is important to assess the degree to which the surface materials depart from ideal Lambertian scattering. Although not directly, MEDA also allows the estimation of the turbulent heat flux through measurements of ground and air temperature, horizontal wind speed, and atmospheric pressure. Thus, MEDA provides a good approximation to the surface energy budget at Jezero crater. Furthermore, MEDA allows the direct determination of thermal inertia for homogeneous terrains using measurements of the surface energy budget and ground temperature without the need for numerical models.

Our main conclusions following the analysis of MEDA measurements for the first 350 sols of the M2020 mission are:

1. Depending on the type of terrain, MEDA-derived *TI* values ranged between 180 (sand dune) and 605 (bedrock-dominated material) SI units. This range is nearly identical to

that at the MSL landing site, with values between 170 and 610 SI units during the first 2500 sols of that mission.

2. The range of variation of collocated THEMIS retrievals was significantly lower, with *TI* values between 295 and 350 SI units. However, there is a good agreement between both datasets when averages over Perseverance's traverse are considered, with values of 350 SI units derived from MEDA and 330 SI units derived from THEMIS. These departures are caused by the different spatial resolution between both datasets (~3–4 m^2 versus 10^4 m^2).
3. There is a very good agreement between MEDA measurements and model (SCM) simulations of each term of the surface energy budget, except for the downwelling atmospheric IR flux. This term is systematically overestimated by SCM. This discrepancy might be caused by the strong diurnal variation in aerosol opacity measured by TIRS, which is not accounted for by numerical models (e.g., SCM).
4. MEDA-estimated values of turbulent heat flux stayed positive through nighttime on certain sols, suggesting lack of thermal inversions. However, this occurred on sols with thermal inertia values significantly higher than the mean value across Perseverance's traverse obtained from MEDA (350 SI units) or THEMIS (330 SI units). This apparent lack of thermal inversion is explained by the small area covered by TIRS (3–4 m^2), which measures ground temperatures not necessarily representative of the surroundings.
5. The albedo presented a marked non-Lambertian behavior on every sol, with lowest values occurring near noon and highest toward sunrise and sunset. The highest albedo values correspond to low phase angles because of the overall backscattering nature of the Martian surface and the onset at smaller phase angles of the opposition effect. The upturn in the phase curves at phase angles > 70° demonstrates the forward scattering nature of some surfaces at high phase angles.
6. Depending on the type of terrain, the daily minimum albedo derived from MEDA ranged between 0.093–0.159. For comparisons, Pancam-derived Lambertian albedos derived at the Opportunity and Spirit landing sites around local noon varied between 0.11–0.22 and 0.14–0.24, respectively. Using numerical modeling, Lambertian albedo values between 0.06–0.28 and of 0.16 were estimated at MSL and InSight, respectively. Thus, Jezero crater is among the darkest landing sites on Mars, in accordance with satellite estimations.
7. The lowest MEDA-derived albedo was recorded during the regional dust storm on sols 312–318 (Ls 152°–156°), when values decreased dramatically due to dust removal and sand transport.
8. Collocated TES orbital retrievals of bolometric albedo in the 0.25–2.9 μm range, performed with a spatial resolution of ~300 km^2 at around 14:00 LTST, showed a value of 0.147 at Jezero crater. While MEDA-derived values at around 14:00 LTST varied between ~0.10 and 0.18 depending on the location, the averaged value across Perseverance's traverse was 0.14, in very good agreement with TES.

The following topics are left open for future investigations: (1) the apparent decrease in thermal inertia during the dust storm, (2) the classification of the geological type of terrain as a function of thermal inertia, albedo and grain size, (3) the analysis of individual phase angle curves as a function of the number and size of the scatterers in the TIRS' FoV (as determined by Mastcam-Z and/or Navcam images), (4) comparisons with bolometric albedos in the 0.25-2.9 μm range

retrieved from OMEGA with a spatial resolution between 1 and 2 km, and (5) analyses of the impact of diurnally varying opacity on thermal profiles at diurnal and seasonal timescales.

The results presented here are key to achieve MEDA's objectives within the M2020 mission, which are to validate model predictions and provide ground-truth to orbital measurements.

Acknowledgments

Germán Martínez wants to acknowledge JPL funding from USRA Contract Number 1638782. A. V. R. is supported by the Spanish State Research Agency (AEI) Project No. MDM-2017-0737 Unidad de Excelencia "María de Maeztu"- Centro de Astrobiología (INTA-CSIC) and by the Comunidad de Madrid Project S2018/NMT-4291 (TEC2SPACE-CM). J. J. acknowledges funding from Mastcam-Z ASU subcontract 15-707. R. H., A. S. L. and A. M. were supported by Grant PID2019-109467GB-I00 funded by MCIN/AEI/10.13039/501100011033/ and by Grupos Gobierno Vasco IT1742-22. F. G. acknowledges financial support from the Agencia Estatal de Investigación of the Ministerio de Ciencia e Innovación and the European Regional Development Fund "A way of making Europe" through project the Centre of Excellence "María de Maeztu" award to the Centro de Astrobiología (MDM-2017-0737), and from the Instituto Nacional de Técnica Aeroespacial through project S.IGS22001. L. M. was supported by CNES and IRIS-OCAV. J. P., M. H., and A.-M. H. are thankful for the Finnish Academy grant #310509. M.-P.Z. was supported by grant PID2019-104205GB-C21 funded by MCIN/AEI/ 10.13039/501100011033. M. de la T. J. acknowledges partial funding from the National Aeronautics and Space Administration (80NM0018D0004). The JPL co-authors acknowledge funding from NASA's Space Technology Mission Directorate and the Science Mission Directorate.

Data Availability Statement

All Mars 2020 MEDA data necessary to reproduce each figure shown in this manuscript are available via the Planetary Data System (PDS) Atmospheres node (DOI: 10.17189/1522849). An exception to this are the LW_d values in the 5–80 μm range (Figs. 8c, 9c, 10 top, 11 top and 15), and the aerosol opacity values derived from TIRS (Fig. 10, middle, and Fig. 11, top). These two datasets re not yet available in the PDS but will be archived at the USRA Houston Repository at the time of publication. THEMIS retrievals of thermal inertia shown in Fig. 7 and TES retrievals of albedo in Fig. 14 can be queried and processed using the open-source JMARS and MASRTHERM software.

References

Apestigue, V., Gonzalo, A., Jiménez, J. J., Boland, J., Lemmon, M., de Mingo, J. R., ... & Arruego, I. (2022). Radiation and Dust Sensor for Mars Environmental Dynamic Analyzer Onboard M2020 Rover. *Sensors*, *22*(8), 2907.

Banfield, D., Spiga, A., Newman, C., Forget, F., Lemmon, M., Lorenz, R., ... & Banerdt, W. B. (2020). The atmosphere of Mars as observed by InSight. *Nature Geoscience*, *13*(3), 190-198.

Bell III, J. F., Rice, M. S., Johnson, J. R., & Hare, T. M. (2008). Surface albedo observations at Gusev crater and Meridiani Planum, Mars. *Journal of Geophysical Research: Planets*, *113*(E6).

Creecy, E., Li, L., Jiang, X., Smith, M., Kass, D., Kleinböhl, A., & Martínez, G. (2022). Mars' emitted energy and seasonal energy imbalance. *Proceedings of the National Academy of Sciences*, *119*(21), e2121084119.

Chide, B., Bertrand, T., Lorenz, R. D., Munguira, A., Hueso, R., Sánchez-Lavega, A., ... Wiens, R. C. (2022). Acoustics reveals short-term air temperature fluctuations near Mars' surface. *Journal of Geophysical Research: Planets* (under review; this issue).

Christensen, P. R. (1988). Global albedo variations on Mars: Implications for active aeolian transport, deposition, and erosion. *Journal of Geophysical Research: Solid Earth*, *93*(B7), 7611-7624.

Christensen, P. R., Banfield, J. L., Hamilton, V. E., Ruff, S. W., Kieffer, H. H., Titus, T. N., ... & Greenfield, M. (2001). Mars Global Surveyor Thermal Emission Spectrometer experiment: investigation description and surface science results. *Journal of Geophysical Research: Planets*, *106*(E10), 23823-23871.

Christian, J. R., Arvidson, R. E., O'Sullivan, J. A., Vasavada, A. R., & Weitz, C. M. (2022). CRISM-Based High Spatial Resolution Thermal Inertia Mapping Along Curiosity's Traverses in Gale Crater. *Journal of Geophysical Research: Planets*, *127*(5), e2021JE007076.

de la Torre Juárez, M., Chavez, A., Tamppari, L. K., Munguira, A., Martínez, G. M., Hueso, R., ... & Rodríguez-Manfredi., J. A. (2022). Diurnal cycle of air temperature fluctuations at Jezero crater. *Journal of Geophysical Research: Planets* (under review; this issue).

Edwards, C. S., Piqueux, S., Hamilton, V. E., Fergason, R. L., Herkenhoff, K. E., Vasavada, A. R., ... & Smith, M. D. (2018). The thermophysical properties of the Bagnold Dunes, Mars: Ground-truthing orbital data. *Journal of Geophysical Research: Planets*, *123*(5), 1307-1326

Elsasser, W. M. (1942). Heat transfer by infrared radiation in the atmosphere. *Harvard meteor. studies*, *6*, 107.

Farley, K. A., Williford, K. H., Stack, K. M., Bhartia, R., Chen, A., de la Torre, M., ... & Wiens, R. C. (2020). Mars 2020 mission overview. *Space Science Reviews*, *216*(8), 1-41.

Fenton, L. K., Geissler, P. E., & Haberle, R. M. (2007). Global warming and climate forcing by recent albedo changes on Mars. *Nature*, *446*(7136), 646-649.

Fergason, R. L., Christensen, P. R., & Kieffer, H. H. (2006). High-resolution thermal inertia derived from the Thermal Emission Imaging System (THEMIS): Thermal model and applications. *Journal of Geophysical Research: Planets*, *111*(E12).

Garrat, J. R. (1992). The atmospheric boundary layer. *Cambridge Atmos. Cambridge Univ. Press*.

Geissler, P. E., Fenton, L. K., Enga, M. T., & Mukherjee, P. (2016). Orbital monitoring of martian surface changes. *Icarus*, *278*, 279-300.

Grott, M., Spohn, T., Knollenberg, J., Krause, C., Hudson, T. L., Piqueux, S., ... & Banerdt, W. B. (2021). Thermal conductivity of the Martian soil at the InSight landing site from HP3 active heating experiments. *Journal of Geophysical Research: Planets*, *126*(7), e2021JE006861.

Guinness, E. A., Arvidson, R. E., Clark, I. H., & Shepard, M. K. (1997). Optical scattering properties of terrestrial varnished basalts compared with rocks and soils at the Viking Lander sites. *Journal of Geophysical Research: Planets*, *102*(E12), 28687-28703.

Haberle, R. M., Houben, H. C., Hertenstein, R., & Herdtle, T. (1993). A boundary-layer model for Mars: Comparison with Viking lander and entry data. *Journal of Atmospheric Sciences*, *50*(11), 1544-1559.

Hamilton, V. E., Vasavada, A. R., Sebastián, E., de la Torre Juárez, M., Ramos, M., Armiens, C., ... & Zorzano, M. P. (2014). Observations and preliminary science results from the first 100 sols of MSL Rover Environmental Monitoring Station ground temperature sensor measurements at Gale Crater. *Journal of Geophysical Research: Planets*, *119*(4), 745-770.

Hébrard, E., Listowski, C., Coll, P., Marticorena, B., Bergametti, G., Määttänen, A., ... & Forget, F. (2012). An aerodynamic roughness length map derived from extended Martian rock abundance data. *Journal of Geophysical Research: Planets*, *117*(E4).

Hueso, R., Newman, C. E., del Rio-Gaztelurrutia, T., Munguira, A., Sanchez-Lavega, A., Toledo, D., ... & Lepinette-Malvite, A. (2022). Convective vortices and dust devils detected and characterized by Mars 2020. *Journal of Geophysical Research: Planets* (under review; this issue).

Johnson, J. R., Kirk, R., Soderblom, L. A., Gaddis, L., Reid, R. J., Britt, D. T., ... & Arnold, G. (1999). Preliminary results on photometric properties of materials at the Sagan Memorial Station, Mars. *Journal of Geophysical Research: Planets*, *104*(E4), 8809-8830.

Johnson, J. R., Grundy, W. M., Lemmon, M. T., Bell III, J. F., Johnson, M. J., Deen, R. G., ... & Squyres, S. (2006a). Spectrophotometric properties of materials observed by Pancam on the Mars Exploration Rovers: 1. Spirit. *Journal of Geophysical Research: Planets*, *111*(E2).

Johnson, J. R., Grundy, W. M., Lemmon, M. T., Bell III, J. F., Johnson, M. J., Deen, R., ... & Squyres, S. (2006b). Spectrophotometric properties of materials observed by Pancam on the Mars Exploration Rovers: 2. Opportunity. *Journal of Geophysical Research: Planets*, *111*(E12).

Johnson, J. R., Bell III, J. F., Geissler, P., Grundy, W. M., Guinness, E. A., Pinet, P. C., & Soderblom, J. (2008). Physical properties of the Martian surface from spectrophotometric observations. *The Martian Surface-Composition, Mineralogy, and Physical Properties*, 428.

Johnson, J. R., Grundy, W., Lemmon, M. T., Liang, W., Bell III, J. F., Hayes, A. G., & Deen, R. G. (2021). Spectrophotometric properties of materials observed by Pancam on the Mars Exploration Rovers: 4. Final mission observations. *Icarus*, *357*, 114261.

Johnson, J. R., W. Grundy, M.T. Lemmon, W. Liang, J.F. Bell III, A.G. Hayes, R.G. Deen, Spectrophotometric Properties of Materials Observed by Mastcam on the Mars Science Laboratory at Gale Crater: 1. Bradbury Landing to Cooperstown, in revision to *Planetary and Space Science*, 2022.

Kahre, M. A., Murphy, J. R., Chanover, N. J., Africano, J. L., Roberts, L. C., & Kervin, P. W. (2005). Observing the martian surface albedo pattern: Comparing the AEOS and TES data sets. *Icarus*, *179*(1), 55-62.

Kahre, M. A., Murphy, J. R., Chanover, N. J., Africano, J. L., Roberts, L. C., & Kervin, P. W. (2005). Observing the martian surface albedo pattern: Comparing the AEOS and TES data sets. *Icarus*, *179*(1), 55-62.

Kieffer, H. H., Martin, T. Z., Peterfreund, A. R., Jakosky, B. M., Miner, E. D., & Palluconi, F. D. (1977). Thermal and albedo mapping of Mars during the Viking primary mission. *Journal of Geophysical Research*, *82*(28), 4249-4291.

Lemmon, M. T., Smith, M. D., Viúdez-Moreiras, D., de la Torre-Juarez, M., Vicente- Retortillo, A., Munguira, A., ... & Apestigue, V. (2022). Dust, Sand, and Winds within an Active Martian Storm in Jezero Crater, *Geophysical Research Letters* (under review; this issue).

Maki, J. N., Bell III, J. F., Herkenhoff, K. E., Squyres, S. W., Kiely, A., Klimesh, M., ... & Lorre, J. (2003). Mars exploration rover engineering cameras. *Journal of Geophysical Research: Planets*, *108*(E12).

Maki, J., Thiessen, D., Pourangi, A., Kobzeff, P., Litwin, T., Scherr, L., ... & Maimone, M. (2012). The Mars science laboratory engineering cameras. *Space science reviews*, *170*(1), 77-93.

Mandon, L., Quantin-Nataf, C., Thollot, P., Mangold, N., Lozac'h, L., Dromart, G., ... & Volat, M. (2020). Refining the age, emplacement and alteration scenarios of the olivine-rich unit in the Nili Fossae region, Mars. *Icarus*, *336*, 113436

Martínez, G. M., Rennó, N., Fischer, E., Borlina, C. S., Hallet, B., De La Torre Juárez, M., ... & Haberle, R. M. (2014). Surface energy budget and thermal inertia at Gale Crater: Calculations from ground-based measurements. *Journal of Geophysical Research: Planets*, *119*(8), 1822-1838.

Martínez, G. M., Vicente-Retortillo, A., Vasavada, A. R., Newman, C. E., Fischer, E., Rennó, N. O., ... & Sánchez-Lavega, A. (2021). The surface energy budget at gale crater during the first 2500 sols of the mars science laboratory mission. *Journal of Geophysical Research: Planets*, *126*(9), e2020JE006804.

Munguira, A., Hueso, R., Sánchez-Lavega, A., de la Torre-Juarez, M., Martinez, G. M., Newman, C., ... & Lorenz, R. (2022, June). Mars 2020 MEDA Measurements of Near Surface Atmospheric Temperatures at Jezero. In *Seventh International Workshop on the Mars Atmosphere: Modelling and Observations* (p. 1509).

Montmessin, F., Gondet, B., Bibring, J. P., Langevin, Y., Drossart, P., Forget, F., & Fouchet, T. (2007). Hyperspectral imaging of convective CO2 ice clouds in the equatorial mesosphere of Mars. *Journal of Geophysical Research: Planets*, *112*(E11).

Newman, C. E., Hueso, R., Lemmon, M. T., Munguira, A., Vicente-Retortillo, Á., Apestigue, V., ... & Guzewich, S. D. (2022). The dynamic atmospheric and aeolian environment of Jezero crater, Mars. *Science Advances*, *8*(21), eabn3783.

Pérez-Izquierdo, J., Sebastián, E., Martínez, G. M., Bravo, A., Ramos, M., & Manfredi, J. A. R. (2018). The Thermal Infrared Sensor (TIRS) of the Mars Environmental Dynamics Analyzer (MEDA) instrument onboard Mars 2020, a general description and performance analysis. *Measurement*, *122*, 432-442.

Piqueux, S., Müller, N., Grott, M., Siegler, M., Millour, E., Forget, F., ... & Banerdt, B. (2021). Soil thermophysical properties near the insight lander derived from 50 sols of radiometer measurements. *Journal of Geophysical Research: Planets*, *126*(8), e2021JE006859.

Polkko, J., Hieta, M., Harri, A.-M., Tamppari, L., Martínez, G. M., Viúdez-Moreiras, D., ... and the MEDA team. Initial results of the relative humidity observations by MEDA instrument onboard the Mars 2020 Perseverance Rover *Journal of Geophysical Research: Planets* (under review; this issue).

Presley, M. A., & Christensen, P. R. (1997). The effect of bulk density and particle size sorting on the thermal conductivity of particulate materials under Martian atmospheric pressures. *Journal of Geophysical Research: Planets*, *102*(E4), 9221-9229.

Putzig, N. E., Mellon, M. T., Kretke, K. A., & Arvidson, R. E. (2005). Global thermal inertia and surface properties of Mars from the MGS mapping mission. *Icarus*, *173*(2), 325-341.

Putzig, N. E., & Mellon, M. T. (2007). Apparent thermal inertia and the surface heterogeneity of Mars. *Icarus*, *191*(1), 68-94.

Putzig, N. E., Barratt, E. M., Mellon, M. T., & Michaels, T. I. (2013, December). MARSTHERM: A web-based system providing thermophysical analysis tools for Mars research. In *AGU Fall Meeting Abstracts* (Vol. 2013, pp. P43C-2023).

Rice, M. S., Reynolds, M., Studer-Ellis, G., Bell III, J. F., Johnson, J. R., Herkenhoff, K. E., ... & Kinch, K. M. (2018). The albedo of Mars: Six Mars years of observations from Pancam on the Mars Exploration Rovers and comparisons to MOC, CTX and HiRISE. *Icarus*, *314*, 159-174.

Rodriguez-Manfredi, J. A., De la Torre Juárez, M., Alonso, A., Apéstigue, V., Arruego, I., Atienza, T., ... & Zurita, S. (2021). The Mars Environmental Dynamics Analyzer, MEDA. A suite of environmental sensors for the Mars 2020 mission. *Space science reviews*, *217*(3), 1-86.

Sánchez-Lavega, A., del Rio-Gaztelurrrutia, T., Hueso, R., de la Torre Juárez, M., Martínez, G. M., ... & Mäkinen, T. (2022). Mars 2020 Perseverance rover studies of the Martian atmosphere over Jezero from 1 pressure measurements. *Journal of Geophysical Research: Planets* (under review; this issue).

Savijärvi, H., & Määttänen, A. (2010). Boundary-layer simulations for the Mars Phoenix lander site. *Quarterly Journal of the Royal Meteorological Society*, *136*(651), 1497-1505.

Savijärvi, H., Martinez, G., Harri, A. M., & Paton, M. (2020). Curiosity observations and column model integrations for a Martian global dust event. *Icarus*, *337*, 113515.

Savijärvi, H. I., & Harri, A. M. (2021). Water vapor adsorption on Mars. *Icarus*, *357*, 114270.

Savijärvi, H. I., Martínez, G., and A.-M. Harri (2022). Surface energy fluxes and temperatures at Jezero crater, Mars. *Journal of Geophysical Research: Planets* (under review; this issue).

Sebastian, E., Armiens, C., Gomez-Elvira, J., Zorzano, M. P., Martinez-Frias, J., Esteban, B., & Ramos, M. (2010). The rover environmental monitoring station ground temperature sensor: A pyrometer for measuring ground temperature on Mars. *Sensors*, *10*(10), 9211–9231.

Sebastián, E., Martínez, G., Ramos, M., Haenschke, F., Ferrándiz, R., Fernández, M., & Manfredi, J. A. R. (2020). Radiometric and angular calibration tests for the MEDA-TIRS radiometer onboard NASA's Mars 2020 mission. *Measurement*, *164*, 107968.

Sebastián, E., Martínez, G., Ramos, M., Perez-Grande, I., Sobrado, J., & Manfredi, J. A. R. (2021). Thermal calibration of the MEDA-TIRS radiometer onboard NASA's Perseverance rover. *Acta Astronautica*, *182*, 144-159.

Shepard, M. K. (2017). Introduction to planetary photometry. *Cambridge University Press*.

Smith, M. D., Wolff, M. J., Spanovich, N., Ghosh, A., Banfield, D., Christensen, P. R., Landis, G. A., and Squyres, S. W. (2006), One Martian year of atmospheric observations using MER Mini-TES, *J. Geophys. Res.*, 111, E12S13.

Smith, M. D., Martínez, G. M., Sebastián, E., Apéstigue, V., Arruego, I., Toledo Carrasco, D., ... & de la Torre Juarez, M. (2022, June). Diurnal and Seasonal Variations of Aerosol Optical Depth at Jezero Crater, Mars. In *Seventh International Workshop on the Mars Atmosphere: Modelling and Observations* (p. 1550).

Spohn, T., Grott, M., Smrekar, S. E., Knollenberg, J., Hudson, T. L., Krause, C., et al. (2018). The Heat flow and physical properties package (HP3) for the InSight mission. *Space Science Reviews*, *214*(5), 33.

Sutton, J. L., Leovy, C. B., & Tillman, J. E. (1978). Diurnal variations of the Martian surface layer meteorological parameters during the first 45 sols at two Viking lander sites. *Journal of Atmospheric Sciences*, *35*(12), 2346-2355.

Toledo, D., Apestigue, V., Arruego, I., Lemmon, M., Gómez, L. G., ... & Sebastián, E. (2022). Dust devil frequency of occurrence and radiative effects at Jezero crater, Mars, as measured by MEDA Radiation and Dust Sensor (RDS). *Journal of Geophysical Research: Planets* (under review; this issue).

Vasavada, A. R., Piqueux, S., Lewis, K. W., Lemmon, M. T., & Smith, M. D. (2017). Thermophysical properties along Curiosity's traverse in Gale crater, Mars, derived from the REMS ground temperature sensor. *Icarus*, *284*, 372-386.

Vicente-Retortillo, A., Martínez, G. M., Rennó, N. O., Lemmon, M. T., de la Torre-Juárez, M., & Gómez-Elvira, J. (2020). In situ UV measurements by MSL/REMS: dust deposition and angular response corrections. *Space Science Reviews*, *216*(5), 1-19.

Vicente-Retortillo, Á., Valero, F., Vázquez, L., & Martínez, G. M. (2015). A model to calculate solar radiation fluxes on the Martian surface. *Journal of Space Weather and Space Climate*, *5*, A33.

Vicente-Retortillo, Á., Martínez, G. M., Renno, N., Newman, C. E., Ordonez-Etxeberria, I., Lemmon, M. T., ... & Sánchez-Lavega, A. (2018). Seasonal deposition and lifting of dust on Mars as observed by the Curiosity rover. *Scientific reports*, *8*(1), 1-8.

Vicente-Retortillo, A., Martínez, G. M., Lemmon, M. T., Hueso, R., Johnson, J. J., Sullivan, R., & ... Rodríguez-Manfredi, J. A. (2022). Dust Lifting Through Surface Albedo Changes at Jezero Crater, Mars. *Geophysical Research Letters* (under review; this issue).

Vincendon, M., Audouard, J., Altieri, F., & Ody, A. (2015). Mars Express measurements of surface albedo changes over 2004–2010. *Icarus*, *251*, 145-163.

Viúdez-Moreiras, D., Lemmon, M., Newman, C. E., Guzewich, S., Mischna, M., Gómez-Elvira, J., ... Bell, J. (2022a). Winds at the Mars 2020 landing site. Part 1: Near-surface wind patterns at Jezero crater. *Journal of Geophysical Research: Planets* (under review; this issue).

Viúdez-Moreiras, D., de la Torre, D., Gómez-Elvira, J., Lorenz, R. D., Apéstigue, V., Guzewich, S., ... Bell, J. (2022b). Winds at the Mars 2020 landing site. Part 2: Wind variability and turbulence. *Journal of Geophysical Research: Planets* (under review; this issue).

Wolff, M. J., Lopéz-Valverde, M. I. G. U. E. L., Madeleine, J. B., Wilson, R. J., Smith, M. D., Fouchet, T., & Delory, G. T. (2017). Radiative process: Techniques and applications. *The atmosphere and climate of Mars*, *18*, 106.

1434 Zhang, Y. F., Wang, X. P., Hu, R., Pan, Y. X., & Zhang, H. (2014). Variation of albedo to soil
1435 moisture for sand dunes and biological soil crusts in arid desert ecosystems. *Environmental earth*
1436 *sciences*, *71*(3), 1281-1288.
1437
1438 Zent, A. P., Hecht, M. H., Cobos, D. R., Wood, S. E., Hudson, T. L., Milkovich, S. M., ... &
1439 Mellon, M. T. (2010). Initial results from the thermal and electrical conductivity probe (TECP)
1440 on Phoenix. *Journal of Geophysical Research: Planets*, *115*(E3).